THE UNIVERSITY OF CHICAGO

SCANNING TUNNELING MICROSCOPY STUDY OF THE REACTION OF ALKANETHIOLATE SELF-ASSEMBLED MONOLAYERS WITH ATOMIC HYDROGEN

A DISSERTATION SUBMITTED TO

THE FACULTY OF THE DIVISION OF THE PHYSICAL SCIENCES

IN CANDIDACY FOR THE DEGREE OF

DOCTOR OF PHILOSOPHY

DEPARTMENT OF CHEMISTRY

BY

JEFFREY D. SAYLER

CHICAGO, ILLINOIS

JUNE 2019

Graduate school is a place to hide for a couple of years

-Michael Eisner

Table of Contents

List of Figures

Acknowledgments

I would like to thank all of the people who helped me complete my PhD in Chemistry at the University of Chicago. First, thank you to my advisor, Professor Steven Sibener, for accepting me into his group and making all of my research possible. I would also like to thank Professors David Mazziotti and Sarah King for serving on my thesis committee.

I must also thank Drs. Qiti Guo and Justin Jureller for all of their support on the MRSEC equipment. Dr. Guo trained me on the first STM that I learned to use, starting me on my path of the technique that I would primarily use for the rest of my PhD research. Thank you also to John Phillips, the lab and building manager, who has worked so hard to keep the building fit to do science in.

Tanya Hagerman has been so much help in helping me navigate the purchasing system, and ensuring that I could buy the supplies necessary for my research. I owe a huge debt of gratitude to Maria Jimenez for keeping the lab running smoothly, for helping me with reimbursements for travel and other expenses, and for all of the myriad other ways that she helps keep the lab running.

I must thank Melinda Moore, Vera Dragisich, and all members of the student services for the department of chemistry. You have done so much in helping me to navigate the chemistry department and the university during my time here.

During the many quarters in which I was a TA for the undergraduate general chemistry class, Dr. Meishan Zhao was such a great help during all of it, from designing and overseeing labs, to handling scheduling and the class roster, to keeping all of the grades in order, and so much more. The undergraduate students interact with him much less than they do the TAs and

professor, but to us TAs Meishan was always the first and usually only person that we turned to for help and support.

For additional help in becoming a better teacher, I would like to thank the Chicago Center for Teaching, as well as all of its instructors, employees, and volunteers. Their classes and workshops did so much to help me improve my teaching. It was refreshing to learn from people who applied a scientific approach to the subject of teaching – who looked for evidence of how to effectively teach, and who recognized that both teaching and learning are do not come naturally, but are rather skills to be learned and practiced.

I owe an enormous debt to all of my coworkers and friends in the Sibener group who have been so instrumental in teaching me how to do science; how to create experiments, analyze data, and draw conclusions. How to set up and use all of the equipment that has been necessary for the research described in this dissertation, write a scientific publication, and of course, how to write this dissertation. All that is true and correct in my scientific publications is due to their help, and any mistakes contained within are mine alone. Of this group, I would especially like to thank Sarah Brown, who has been my partner in all of the research that I am presenting here. I would also like to thank Darren Veit, who joined this lab at the same time I did, and who has been a source of great support as we have gone through our graduate school adventure together.

Finally, I would like to thank my parents, for their encouragement along the way. Most importantly, I must thank my girlfriend, Maggie Naden. Her love for me and her support of me has been the single most important thing in my life during my time in graduate school, and there are no words adequate to express how much her support has meant to me for so long.

Abstract

The effect of both chain length and temperature on the reactivity of alkanethiolate self-assembled monolayers (SAMs) with atomic hydrogen was studied *via* direct imaging of the surface throughout the reaction. These images were obtained with a ultra-high vacuum scanning tunneling microscope (UHV-STM) with a thermal gas cracker allowing for *in situ* exposure to atomic hydrogen.

For a series of alkanethiolate SAMs 8- to 11- carbon atoms long (8C-11C), it was found that small increases in chain length caused disproportionately large decreases in reactivity at room temperature. This reaction progression was described by an exponential function with two rates: a slow rate for hydrogen reacting with standing-up phase, which is dependent on chain length, and a fast rate for low-density phase reactions, which is the same for all samples. Additionally, with the ability of the STM to observe molecular-scale changes in surface morphology, chain-length dependent changes in the sample were seen. For the shorter chain 8C and 9C samples, there was a significant growth in the average etch pit area over the course of the reaction, while few changes were seen in the 10C and 11 C samples.

For decanethiol, it was found that decreases in the temperature of the SAM during exposure to atomic hydrogen caused corresponding decreases in the rate of the reaction. Additionally, it was found that between 250 K and 270 K the alkanethiolate molecules became immobile on the surface. The reaction at 270 K appears to proceed via the same pathway as at room temperature, while during the reaction at 250 K the surface evolves in a new manner. The same two-rate model was applied to the temperature-varied reactions. At 270 K and 290 K the model described the reactivity relatively well, suggesting that lowering the amount of thermal

energy available in the SAM by lowering the is energetically equivalent to raising the intermolecular forces by increasing the chain length. When applied to the 250 K experiment, the model seems to describe the initial reactivity, when the slow rate dominates, but poorly describes the later, faster parts of the reaction, probably due to the lack of alkanethiolate mobility.

Chapter 1: Introduction

Gas-surface reactions are a broad class of reactions describing any case where a molecule from the gas phase impinges upon and reacts with a solid surface. They form the basis for the degradation or passivation of different types of materials. Treatment with reactive oxidizing gaseous compounds such as ozone and chlorine dioxide is used to disinfect surfaces. Our lab has studied the reaction of atomic oxygen with nerve agent simulants to investigate the possibility of decontamination with reactive gas species after a chemical attack.[1,2] Collisions of gas-phase molecules with surfaces is an extremely frequent occurrence: at room temperature and pressures, atmospheric gasses collide with a square centimeter of surface approximately 10^{24} times per second. Most of these reactions, of course, result in the gas molecules reflecting from the surface without reaction. Occasionally, however, reactive gas species can react with surfaces.

The gas-surface reactions taking place in environmental conditions are complicated by the sheer number of collisions taking place from many different molecules, as well as the heterogeneity and poor characterization of most surfaces. In this thesis, I will describe two sets of experiments to study a certain type of gas-surface reaction, under much more controlled conditions than is typical under atmospheric pressure and ambient conditions.

In the following chapters, I will discuss experiments to study the reaction of atomic hydrogen (H) with alkanethiolate self-assembled monolayers (SAMs). These experiments are conducted under ultra-high vacuum (UHV) conditions, in order to minimize unwanted gas collisions with the surface. Alkanethiolate SAMs are a well-characterized and extensively studied systems, which form ordered surfaces, creating a less complicated system to study the interaction of actomic H with an organic surface.

The remaining sections of this chapter serve as an introduction to the type of reaction that I have studied: atomic hydrogen reacting with alkanethiolate SAMs; the surfaces that I studied: SAMs; and the primary technique used to study these reactions: scanning tunneling microscopy (STM). In **Chapter 2**, I discuss the details of the instruments used in carrying out these experiments, as well as the mechanics of processing the data and building a model to explain the data. In **Chapter 3**, I go over the first set of experiments that we conducted to investigate the reaction of hydrogen atoms with alkanethiolate SAMs. In these experiments, we expose 4 different alkanethiolate SAMs of increasing thickness to atomic hydrogen, and monitor the course and rate of the reactions with STM. Finally, in **Chapter 4** I describe experiments undertaken at different temperatures with a single type of alkanethiolate SAM, to better understand the mechanism of the reaction and to measure the effects of temperature on the rate of reactivity.

1.1 Gas-Surface Reactions of Alkanethiolate SAMs

The reactions of reactive gases with organic layers is an important degradation mechanism in organic layers. These reactions may change the physical and chemical properties of the layers, which may be detrimental to the purpose of the organic layer. These gas-surface reactions may be quite complex, with multiple reactive species creating a multitude of possible products. Studies of simplified, model layers reacting with a variety of reactive gas species have been conducted to give insight into their reactivity[3–10].

Thiolate self-assembled monolayers (SAMs) form well-ordered, well-studied, tunable organic surfaces. For these reasons, SAMs make good model systems for studying a variety of

reactions on and with different organic surfaces, including the reaction of reactive gases with organic surfaces. SAMs and other organic layers are also sometimes used in order to passivate a reactive surface towards gas species.[11] The reactions of SAMs and other thin organic layers with atomic hydrogen[12], atomic oxygen[13–16], atomic chlorine[5,17], and other reactive species[6] have been studied in some detail, and the work presented in this thesis continues the study of reactions between atomic hydrogen and alkanethiolate SAMs.

Atomic hydrogen, chlorine, and oxygen react with alkanethiolate SAMs via different mechanisms. The oxygen and the chlorine, being comparatively large atoms, cannot penetrate far into the organic layer of the SAM. Therefore, they react with the alkane tails of the SAMs via radical hydrogen abstraction, eventually giving rise to various cross-linking reactions and slow erosion of the organic layer. Atomic hydrogen on the other hand is a smaller atom, and has a considerably easier time penetrating into the ordered alkane chains of the standing-up phase.

The reaction of atomic hydrogen with alkanethiolate SAMs was studied by X-ray photoelectron spectroscopy (XPS) by Fairbrother and his co-workers, who investigated the rate and mechanism of reactivity.[12] They found that for relatively short chain alkanethiolate SAMs, with 12 carbon atoms or fewer, the predominant reaction pathway is for the atomic hydrogen to make its way down to the gold surface, and hydrogenate the sulfur atom of the alkanethiolate, breaking the gold-sulfur bond. The alkanethiol then leaves the surface intact. For alkanethiolate SAMs with longer alkane chains (16 carbons or greater), very few hydrogen atoms are able to reach down all the way to the gold surface. Instead, they react with the alkane chains via hydrogen abstraction, similar to how the atomic oxygen and chlorine does even with short-chain alkanethiolate SAMs. This reaction pathway is much slower than the hydrogen recombining

with sulfur at the surface. The exact chain length at which the reaction pathway shifts from primarily being at the gold-sulfur bond to being along the alkane backbone is unknown, occurring somewhere between 12 and 16 carbon atoms in length.

The XPS studies of these systems are powerful ways of understanding the reaction of atomic hydrogen with alkanethiolate SAMs. However, they are limited in that they only give information about the surface as an average over a macroscopic area. SAMs, though they order into well-defined crystal domains, do have defects, grain boundaries, etch pits, and step edges on the underlying substrate, creating a non-uniform surface on the nanometer scale. We might expect that the reaction of atomic hydrogen will react differently at defect sites, rather than on well-ordered domains. In order to track the reaction of gas species with SAMs on this very local scale, scanning tunneling microscopy is used to image the surface as the SAM reacts and is removed.

A series of experiments by Kautz and Kandel and their co-workers have elucidated the general course of the reaction of an alkanethiolate SAM with atomic hydrogen.[16,18–21] This may be seen in our work in **Chapter 3**, where **Figure 3.1** shows the progression of an alkanethiolate SAM under increasing exposure to atomic hydrogen. The first visible signs of reactivity are seen by a widening of the grain boundaries. Eventually, larger patches of area where the standing-up phase has been removed become visible, and appear topographically lower. As these patches of not-standing phase grow, domains of lying-down phases can sometimes be seen within them. The reacted areas grow larger and link up, eventually leaving large areas of reacted SAM surrounding patches of remaining standing-up phase. These patches shrink, and eventually completely disappear. As this happens, small gold islands begin to appear on the surface. These

are the former gold-adatoms that were incorporated into the SAM. After enough of them have been liberated by the reaction of their attached thiol molecules, they coalesce with each other on the surface.[19]

Some observations can be made about this reaction based on the images. It certainly appears that the reaction of atomic hydrogen with a SAM preferentially takes place at defects such as grain boundaries and etch pits. It is these areas that show the earliest signs of reaction. This would also explain the changing rate of the reactivity. As the SAM becomes more and more reacted, the rate at which it continues to react increases. This makes sense, as the surface becomes more defected as the reaction progresses, presumably opening up more sites for further reaction to occur. However, some qualifications must be made in describing the reaction in this way. At room temperature, alkanethiolate molecules on a gold surface are mobile.[22] This explains, for example, why as the density of the SAM is reduced throughout the reaction, some of the molecules form lying-down phase. It also means that it's possible that some alkanethiolate molecules that are in a pristine standing-up phase are in fact reacted, and then the remaining molecules rearrange to close the gap left by the departing molecule, and minimize the overall energy. However, there are several pieces of evidence, as discussed in the following two chapters, that convinces us that most of the reactivity does indeed take place at defected sites on the SAM.

Insight into the reactivity of SAMs can also be gained by examining the temperature-dependence of reaction rates and pathways. At lower temperatures, the alkane tails of the SAM should have reduced thermal motion, and should form a more well-ordered crystal in the standing-up domains. Additionally, at a certain temperature, the thiolate molecules on the

surface should become immobile, which would give a much clearer picture of exactly how the reaction occurs. Within our lab in the past, some investigation was done on the rate of reactivity of atomic oxygen with several alkanethiolate SAMs at different temperatures.[23] Unsurprisingly, the rate of reaction with both 11-carbon and 16-carbon alkanethiolate SAMs decreased as the temperature was lowered from room temperature to 150 K. More surprisingly, the effect that temperature had on the two SAMs was not the same magnitude. The rate of reaction with the 11 carbon SAM decreased only modestly, while the reaction with the 16 carbon SAM was nearly completely shut down. It was thought that even though the amount of thermal energy was reduced, the 11 carbon SAM still exhibited some disorder even at the lower temperature, while the 16 carbon SAM, featuring stronger van-der-Waals forces between individual molecules, froze into a much more perfect crystal. Chapter 4 explores the effect of temperature on the reaction of atomic hydrogen with alkanethiolate SAMs.

1.2 Alkanethiolate Self-Assembled Monolayers

All of the experiments described in this thesis are conducted on alkanethiolate self-assembled monolayers (SAMs) on the (111) face of gold. Thiolate SAMs are extremely well-studied systems, and have been used in a variety of applications where a chemically adhered surface with well-defined structure is desirable. The properties of thiolate SAMs can be modified by changing the nature of the molecular group on the thiol, making a system that allows for tunable modification to surface properties. These properties that can be controlled include reactivity, wetting, adhesion, and photoactivity.

Alkanethiolate SAMs were first described in 1983[24], just a few years before the first STM was invented. Since then, scanning tunneling microscopy has been one of the primary (though certainly not exclusive) techniques used to investigate them. The molecular structure of SAMs was extensively studied by STM, as has been their mechanism of formation, their stability, and phase diagrams at different densities[22,25–30].

Thiolate SAMs consist of a sulfur group, which bonds to the gold surface, and a carbon tail that sticks away from the surface. In the case of alkanethiolate SAMs, the tail is just an alkane group that may be different lengths (ethanethiol, octanethiol, octadecanethiol, etc.), though various functional groups may also be incorporated into the tail to change the properties of the surface.[31–35]

Alkanethiolate SAMs form several distinct phases on the gold surface, depending on the density of thiol molecules on the surface as well as the method of preparation. The most dense phase is a close-packed hexagonal structure, the $\sqrt{3}\times\sqrt{3}$ phase, which sometimes shows a $c(4\times2)R30^{o}$ superlattice. The formation of this phase is self-limiting, meaning that surfaces covered in this phase are easily formed via solution deposition of thiols on to gold, or vapor-phase deposition, assuming that the gold is exposed to the thiolate long enough for it to fully form this phase. The alkane tails in this phase pack together and are tilted ~ 32^{o} from the surface normal, which gives the highest degree of contact between the tails and the strongest adhesion due to van der Waals interactions between the alkane tails (**Figure 1.1**). There are three degenerate directions on the Au(111) surface, and therefore three degenerate possible directions for the alkane tails to be tilted.

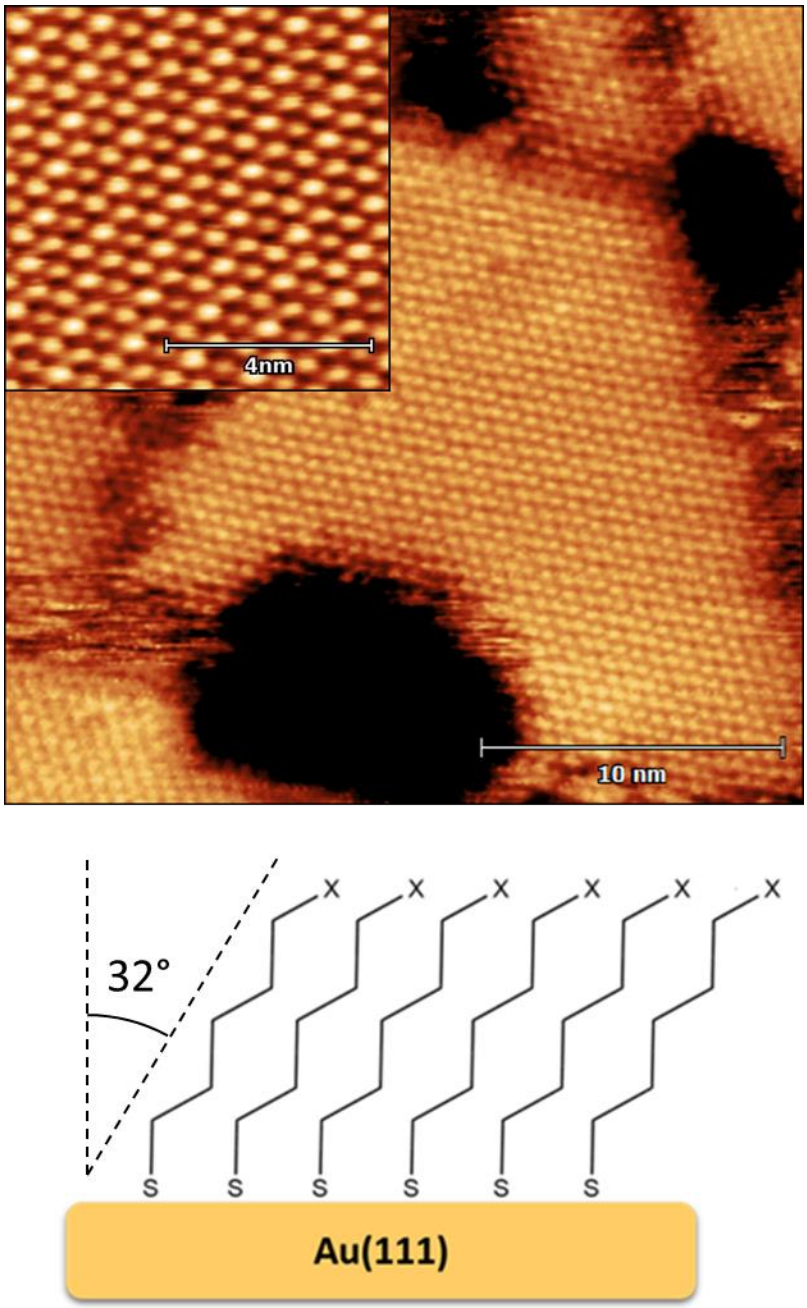

[Figure 1.1] (Top) An STM image showing a domain of close-packed standing phase of a decanethiolate SAM. Grain boundaries are seen separating the area from neighboring domains. **(Inset)** An enlarged area of the standing phase, showing the hexagonal structure. The c(4×2)R30^{o} superlattice can also be seen faintly. **(Bottom)** Diagram showing an alkanethiolate SAM with the alkane tails tilted relative to the surface normal in order to achieve a more favorable packing..

When the thiol molecules form the standing-up phase on the surface, they organize into domains, separated by boundaries from other crystal domains where the alkane tails lie in a different direction. Separating the domains are domain boundaries, and at the intersection of domain boundaries there are gold vacancy islands, or etch pits, which consist of small areas that are one atomic step height of gold lower than the surrounding atomically flat terrace. The sizes and density of both the alkanethiolate domains and the etch pits vary based on the method used to prepare the SAM, as well as any annealing conditions. In general, the etch pits are roughly circular and have diameters on the order of 5 nm. The standing SAM domains are on the order of 20 nm across, with domain boundaries that are often fairly straight, especially when the SAM is formed by vapor deposition.[18]

Historically, there has been some debate about the structure of the gold surface under a SAM, and how the etch pits are formed.[36–45] It now appears that gold atoms are removed from the surface when thiol molecules bond to the substrate, and become incorporated into the SAM. Work by Kautz and Kandel showed that gold atoms are incorporated into the standing-up phase of the SAM at a ratio of one gold atom to two thiol molecules.[18,19] There are a number of proposed models for the exact structure, but it suffices to say that this is the origin of the etch pit formation, and also that when the thiol molecules are removed, as is done in the work presented in this thesis, these gold adatoms are re-deposited onto the surface.

When alkanethiolate molecules exist on a gold surface at densities lower than that of the standing-up phase, several different lower-density phases form. In these phases, the alkane tails do not stand up away from the surface, but instead lie on the gold surface.[28,29] The sulfur head groups associate with each other and form lines on the surface, so these phases are referred to as

lying-down or striped phases. These lying-down phases can be prepared by depositing fewer alkanethiol molecules onto the gold surface during formation of the SAM (by solution deposition from a very dilute solution[46], or vapor deposition for shorter periods of time). They can also be formed by starting with a surface covered in standing-up phases, and removing some of the alkanethiolate molecules via heating, or reaction with atomic hydrogen[20], as I describe later in this thesis.

1.3 Scanning Tunneling Microscopy

The principle technique used for obtaining data in the experiments presented in this thesis is scanning tunneling microscopy (STM). Since its invention in 1982[47], STM has rapidly become a favorite and powerful technique for investigating conductive surfaces. STM images a surface on an atomic scale, allowing for investigation of single-molecule phenomena, unlike most traditional surface-science techniques that give ensemble information about a surface[48–50].

STM relies on the principle of quantum tunneling to probe the electronic structure and create images of the surface. A small electrical potential is applied between the surface and the tip, and the tip is held close to the surface (within several angstroms). The vacuum or gas between the tip and the sample has a much higher electrical potential than the metal surface and tip, and so classically, current flow is forbidden, even though there is a difference in potential. However, in quantum systems the electron's wave function remains non-zero even in classically-forbidden areas, meaning that the electrons will tunnel from the area with lower voltage to the area with higher voltage, across the gap. **Figure 1.2** contains a simplified schematic of the electrical circuit used for STM.

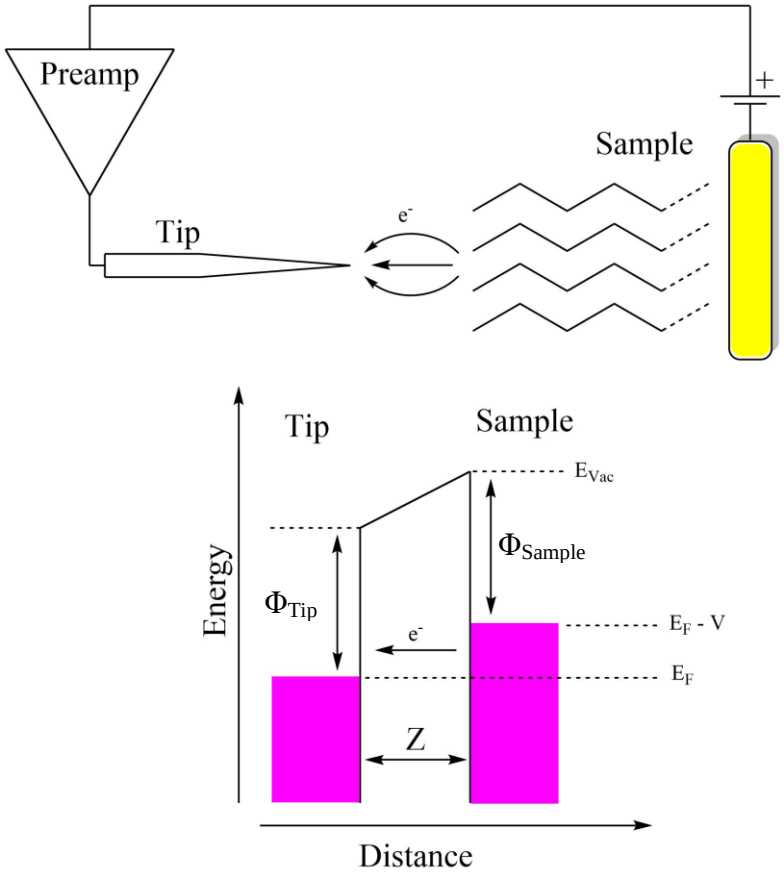

[Figure 1.2] (Top) A simplified electrical diagram of quantum tunneling in the STM. A bias between the sample and the tip causes electrons to tunnel over the vacuum gap. The small current is converted to a voltage with a current-sensitive preamplifier that is read by the instrument control and used for the constant-current feedback loop. **(Bottom)** An energy diagram of the tunneling junction with a negative bias applied to the sample.

The rate of electron tunneling can be found using the Wentzel-Kramers-Brillouin (WKB) approximation, which assumes that when an electronic potential is slowly varying, then the amplitude of the wave function within the potential will also vary slowly. This gives an expression for the current as follows:

$$I = \int_0^{eV} \rho_s(E)\rho_t(eV - E)T(E, eV)dE \qquad (1.1)$$

The current is dependent on the voltage applied to the sample (V), density of states (DOS) of both the tip and sample (ρ_s and ρ_t), as well as the transmission function T, which is as follows:

$$T(E, eV) = \exp\left(-\frac{2Z\sqrt{2m}}{\hbar}\sqrt{\frac{\phi_s+\phi_t}{2}+\frac{eV}{2}-E}\right) \qquad (1.2)$$

The transmission function is exponentially dependent on the length of the vacuum gap, as well as the barrier height[51].

Ignoring the effect that the non-uniform density of states of both the tip and sample have on the rate of tunneling, as well as the small effect that the applied voltage has to the barrier height, the tunneling current is linearly dependent on the difference in voltage, and exponentially dependent on the distance between the sample and the tip. The exponential dependence of current with respect to distance means that the current is extremely sensitive to the area that is directly under the very end of the STM tip, allowing in the best cases for resolution of around an angstrom, giving atomically resolved images.

The position of the STM tip is controlled with a piezoelectric tube. Piezoelectric materials are compounds with an intrinsic polarization, such that when a mechanical force is applied, a voltage develops. The reverse is also true: when a voltage is applied, the material bends slightly. With a piezoelectric tube, the x, y, and z position of the tip can be controlled very precisely with the application of modest amounts of voltage. In our microscope, each volt applied in the x or y direction shifts the tip by 20 nm, and with a maximum voltage of 215 V, the horizontal range of motion is about a micrometer. The best-case resolution from the piezo positioning in the horizontal directions is about an angstrom. In the vertical direction (the z-

direction) the motion is much smaller, 0.75 nm/V. The resolution of the instrument in the z direction is also much better, on the order of 0.1 angstrom.

When using a scanning tunneling microscope for imaging a surface, the tip is rastered over the surface, creating a series of lines which are stacked to form the image. During imaging, two pieces of information are collected for each point on the image. The first is height, how far extended or retracted the piezo tube is relative to its neutral position (in practice, it is the voltage applied to the piezo tube that is recorded and converted to a height using the sensitivity of the piezo tube). The second is the current flowing between the sample and the tip. Therefore, two images are created: a topographic image, created by displaying the height values of the image, and a current image.

A proportional-integral (PI) feedback loop controls the tip z-position as a function of the current. A current setpoint is set by the user, and the controller either extends the tip closer to the sample, to increase the current, or pulls the tip further from the sample to decrease the current, in order to try to maintain the current at the setpoint. There are two modes that STM imaging may be taken in: constant current and constant height. Constant current mode is the more typical method of obtaining images, and is exclusively used to take the images for the experiments described in this thesis. In this mode, the PI loop is set to be as responsive as possible (without introducing further noise or ringing), and the tip moved slowly enough across the sample, that the tip is able to follow the contours of the surface faithfully, and the current image is fairly flat. In constant-height mode, the PI loop is turned down or off, so that the tip maintains a constant extension of the piezo tube. As the surface gets closer or further from the tip due to the topography of the sample, the current correspondingly gets larger or smaller. In

this case, the current image contains nearly all of the information, and the height image remains fairly flat.

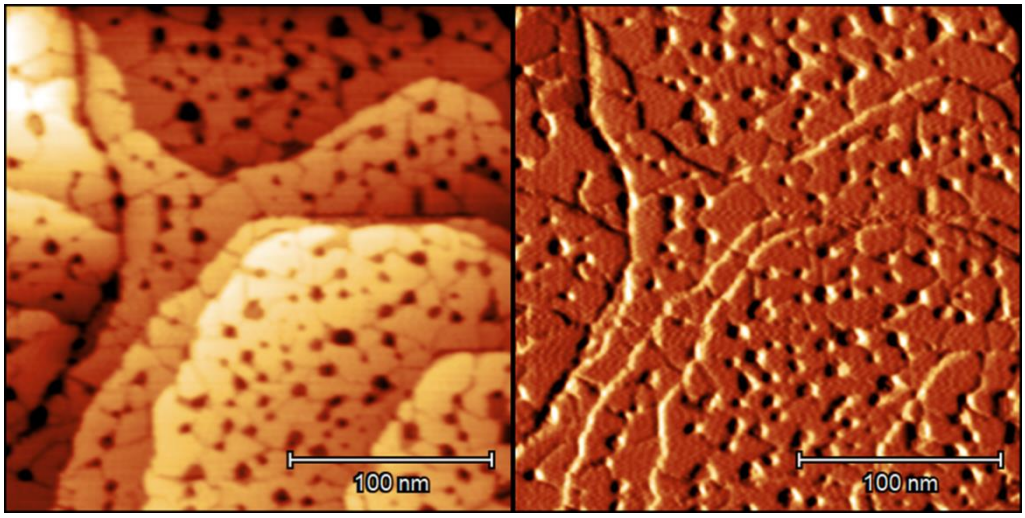

[Figure 1.3] Topographic (left) and current (right) images taken of a decanethiol SAM. The STM was in constant-current mode during the acquisition of these images. The image on the left is therefore an accurate representation of the topography (possibly modulated by differing electronic density of states in the sample), while the image on the right is the error signal from the feedback loop maintaining a constant tunneling current. It is clear from the current image that the STM tip was being moved from left to right across step edges: when stepping up, a high current is momentarily created before the feedback loop corrects it, while when stepping down, a low current appears briefly. STM imaging conditions were 0.7V, 10 pA.

The density of electronic states on the sample also strongly affects the current while tunneling (the metal tip has a relatively flat density of states, and so is generally not considered). When the surface is placed at a positive potential relative to the tip, electrons tunnel from the tip into empty states on the surface. Conversely, when the surface is put at a negative potential, electrons tunnel from the filled states on the surface into the tip. The density of states therefore adds another term to the current tunneling between the tip and the sample, in addition to the height and voltage. For this reason, the height image of an STM image is not necessarily truly representative of the physical topography of the sample. Areas of the image that have a high

density of states relative to their surrounding area (a dangling bond, for example) will show up as higher than the surrounding area, at least when imaging at voltages where the relevant density of electronic states contributes to the current. However, this does not mean that no topographic information can be understood from the height images. When imaging two locations of the same type of surface, the electronic structures will be the same for both, so differences in the height image directly correspond to differences in the actual topography. Additionally, the heights of features due to different electronic structures will typically change when the imaging bias is changed, while height features due to actual topography will stay relatively the same.

This dependence of current with the electronic structure, while a slight hindrance to interpreting images, allows a method for interrogating the electronic density of states with a scanning-tunneling microscope, known as scanning tunneling spectroscopy (STS)[51]. In brief: the tip is brought into tunneling range of the sample, and then is held in place. The bias on the sample is ramped several volts, and the tunneling current recorded as a function of bias voltage. The derivative of the tunneling current with respect to voltage is strongly dependent on the electronic density of states, giving insight into the electronic structure of the sample beneath the tip. No STS measurements were taken in the course of the experiments described in this thesis, though the microscope used for this thesis is capable of, and has been used to take such measurements.[52,53]

Chapter 2: Experimental Methods and Instrumentation

2.1 Instrument Design

All of the experiments described in this thesis were obtained on an ultra-high vacuum scanning-tunneling microscope (UHV-STM). A picture of the chamber and attached instruments is contained in Figure 2.1. The setup consists of three chambers, separated by gate valves. Samples are loaded via the load lock, pumped by a turbomolecular pump backed by an oil-free scroll pump, down to a pressure of around 1×10^{-8}. A transfer arm is used to transfer the sample into an STM chamber, and a sample preparatory chamber, both of which are pumped by a Gamma Vacuum TiTan 200L ion pump, down to a pressure of about 5×10^{-11} torr.

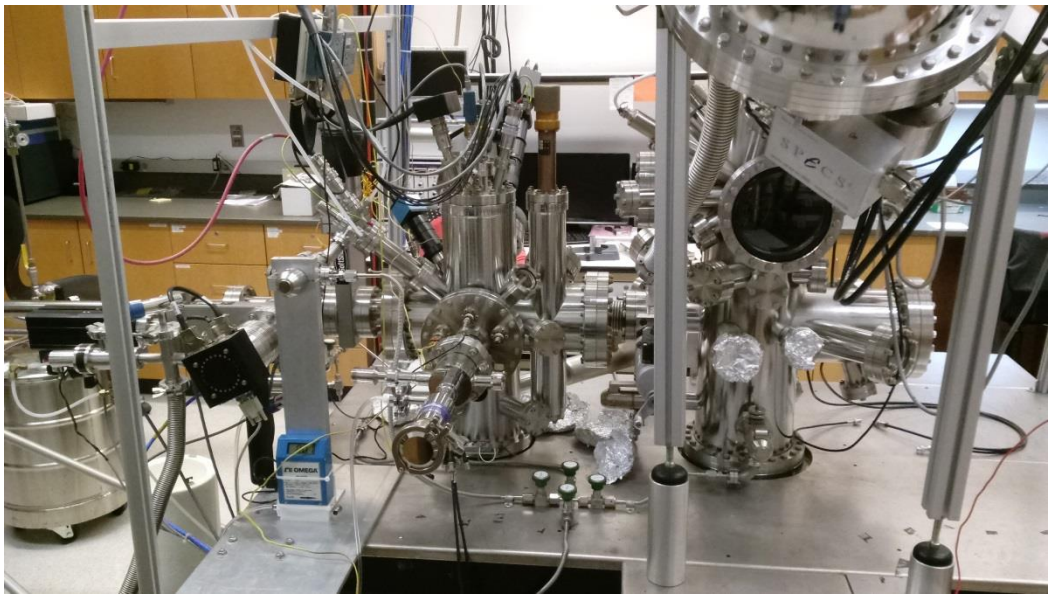

[Figure 2.1] A picture of the instrument in which all of the experiments described within this thesis were conducted. On the far left is the load lock and turbomolecular pump, in the middle the imaging chamber, and on the right the preparatory chamber. The transfer arm used for moving samples between chambers can be seen on the far left.

The imaging chamber contains a variable temperature RHK UHV 350, beetle style Atomic Force Microscopy/Scanning Tunneling Microscope (AFM/STM). The AFM/STM is capable of imaging from around 20 K with liquid helium to 373 K.

Also contained in the imaging chamber is the Mantis MGC-75 thermal gas cracker (**Figure 2.2**), pointed directly at the sample when it is in the stage for imaging, and about 8 cm away from the surface. The gas cracker is oriented at 50° from the surface normal. In the gas cracker is a 3 mm diameter iridium tube, which the hydrogen gas passes through on its way into the chamber. This tube is heated to about 2000 K by electron bombardment from a nearby filament, meaning that any hydrogen that touches the tube during its passage into the chamber is thermally dissociated. For low hydrogen flow rates, the gas cracker is quite efficient, splitting around 95% of the hydrogen.

[Figure 2.2] A picture of the thermal gas cracker, before it was mounted in the UHV chamber. The heated iridium tube that cracks hydrogen and oxygen is contained in the copper cylinder on the right.

The thermal gas cracker is water cooled, requiring a flow of at least 0.5 L/min in order to properly cool it. The gas cracker is cooled by the process water in the building, which typically has a temperature around 18-20 °C. The water flow is monitored with a flowmeter, and

controlled manually with a valve. To provide protection for the gas cracker in the case of a water stoppage, a flow interlock is in the line hooked to the gas cracker control, which will shut off power to the gas cracker if the water flow is interrupted or falls below about 0.6 L/min.

The hydrogen gas for the gas cracker is supplied from a lecture size gas bottle, equipped with a regulator, which is directed through pipes with VCR fittings to the gas cracker. The forelines are pressurized to a few PSI of hydrogen, which is then let into the gas cracker and chamber through a leak valve.

The sample stages in both the STM/AFM and preparatory chambers allow for cryogenic operation, as well as heating to over 1500 K. The preparatory chamber has an X-ray gun and hemispherical electron analyzer for conducting X-ray photoelectron spectroscopy (XPS) measurements, an electron gun for auger electron spectroscopy (AES), and argon ion sputtering.

Samples are mounted into pucks, shown in **Figure 2.3**, containing electrical connections to the sample for applying a bias voltage to the sample for imaging, a K-type thermocouple for monitoring sample temperature, and a filament underneath the sample for radiative or electron bombardment heating. STM and AFM tips are transferred into and out of the microscope with similar types of pucks. A combination of up to six tips and samples may be stored in the sample elevator contained in the STM chamber.

2.2 Alkanethiolate SAM Preparation

Alkanethiols (1-octanethiol, 1-nonanethiol, 1-decanethiol, 1-undecanethiol) are commercially purchased from Sigma-Aldrich and used without further purification. Absolute ethanol (ACS Reagent Grade, >99.5%) is also purchased from Sigma-Aldrich and used without

further purification. The alkanethiolate SAMs are prepared on substrates of 150 nm layers of Au(111) deposited onto cleaved mica, purchased from Agilent, and later Keysight Technologies. The gold substrates are bought in 1 cm × 1 cm sizes, and cut into squares approximately 5 mm × 5 mm before use. The gold is annealed under a hydrogen flame, in order to remove contaminants and increase the area of the terraces. The gold forms atomically flat terraces of up to hundreds of nanometers, and domains up to several microns.

To prepare the SAMs, 1 mM solutions of each of the alkanethiols is prepared in ethanol. The annealed gold substrates, after cooling, are placed face-up on the bottom of a vial containing the alkanethiol solution, and then annealed in a temperature-controlled oven at 60^{o}C for 2.5 hours, to allow the SAM to fully form into the thermodynamically-favored standing-up phase. The SAMs composed of each of the four different alkanethiols form similar surface morphologies. The alkanethiolate molecules bond to the surface and form well-ordered domains of close-packed standing-up phase on the order of 20 nm, separated by grain boundaries where domains of different orientation meet. Gold vacancy islands – etch pits – form at the intersection of domain boundaries.

After annealing in the ethanol solutions, the SAMs are allowed to cool to room temperature in their solutions, and then removed and rinsed 10 times on each side of the substrate with ethanol, and then allowed to dry by evaporation in the air. The rinsed and dried SAM was then mounted in the RHK sample puck, placed into the load lock, pumped to UHV pressures, and transferred into the STM chamber for imaging and reaction. The time the SAMs were allowed to sit in air, out of their solution, was generally kept to under 30 minutes, in order to limit the amount of degradation of the SAM in the air. (SAMs would generally be stable and

imagable if left in the air for up to a couple days or more. However, they would begin to degrade, which could look similar to the types of reactivity with atomic hydrogen that we were measuring.) While in vacuum, the ion pressure gauges in the chamber containing the SAMs are left off, as stray electrons or ions might degrade the SAM[54]. The windows of the chamber are also kept covered with aluminum foil while not doing experiments, to minimize the exposure of the SAMs to light. It is not clear if this was necessary, though it is known that light assists with the degradation of alkanethiolate SAMs, at least in air.[55]

For the reactions described in **Chapter 3**, all of the samples actually consisted of two SAM samples, mounted side-by-side in the sample puck (see **Figure 2.3**). The reason for this is to ensure that proper relative reactivity rates were attained, even if from day to day there is some variability in the atomic hydrogen flux. In order to fit both samples into one puck, the gold on mica pieces were cut to a size of about 3 mm × 5 mm, narrower than the 5 mm × 5 mm squares used when a single sample is mounted.

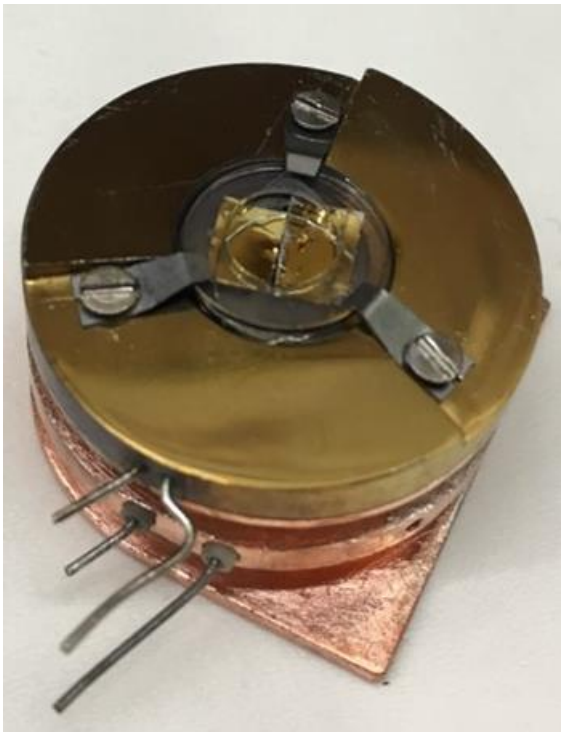

[Figure 2.3] The sample holder used for the experiments described in this thesis, with a dual sample mounted, as used for the experiments in **Chapter 3**.

Tunneling conditions for imaging the SAMs varied somewhat, based on the specific sample and tip. In general, the alkanethiolate monolayers are imaged with a bias on the sample of about +0.7 V, with a setpoint current of 5-50 pA. Above 50 pA, the STM tip begins to get too close to the sample, interfering with alkane tails of the monolayers and degrading the image, while below 5 pA the instrument noise becomes too significant. The longer chain lengths are typically imaged with lower setpoints within this range, as the longer tails cause the tip to begin to reach the alkane tails at lower setpoints.

2.3 Temperature Control

Most of the reactions presented in this thesis were carried out at room temperature, without any temperature measurement on the sample or any active temperature control. The lab temperature was generally between 20-24 °C (293-297 K).

For the experiments that were run at reduced temperatures, the temperature was measured and controlled much more closely. The temperature on the sample was monitored by a K-type thermocouple (chromel-aluminel) on top of the sample. The thermocouple was connected to a Lakeshore 331 Temperature Controller, which also contains the PID loop to control the temperature, as described below. The sample was cooled by running liquid nitrogen through the Cryo Industries continuous flow cryostat, while measuring the volume flow of the exhaust gas. While initially cooling, the valve on the liquid nitrogen is adjusted such that the exhaust flows at around 4 L/min, though while holding the temperature steady the flow rate was reduced to around 2L/min.

If allowed to run unchecked, the liquid nitrogen in the cryostat will cool the sample stage to around 110 K. In order to control the sample temperature, variable heating is applied to the sample while also cooling. The heating is applied through radiant heating from underneath the sample by running 1-2.5 A through a tungsten filament mounted in the sample puck.

The filament was powered by a Lambda power supply, which was in turn controlled by the Lakeshore 331 temperature controller. The Lakeshore only had a current-controlled output, so in order to convert that to the voltage input needed for the power supply, two 100 Ω control resisters are placed across the Lakeshore output. Typically, around 2 A was needed to keep the temperature at the desired level, either 250 K or 270 K.

The sample was allowed to stabilize at its target temperature for an hour or more before imaging. If the sample temperature was still too unsteady, the STM imaging would show heavy thermal drift. Once stable, the Lakeshore would control the temperature to within several hundredths of a Kelvin.

2.4 Reaction Methodology

Before starting to react a new SAM with atomic hydrogen from the thermal gas cracker, the forelines of the gas cracker are pumped out with the scroll pump, and then flushed with hydrogen from the lecture bottle, to ensure that only hydrogen is in the foreline, and that other gases are not being introduced through the gas cracker that might confound the experiment.

Once a new SAM sample of the appropriate chain length has been prepared and loaded into the imaging chamber, it is imaged (described below in **Section 2.5**) to ensure that the sample is well-ordered, and to collect data for the initial datapoint in which the sample has yet to be reacted with atomic hydrogen.

Once these initial images are taken, if the sample is going to be held at a temperature other than room-temperature during the reaction, the sample is brought to the target temperature, as described in **Section 2.3** above. If this is done, once the sample is stable, additional images are taken at the target temperature, in order to ensure that imaging at the experimental temperature is working well.

To carry out the reaction with hydrogen, the scan head is retracted from the surface, and then pulled up off of the sample puck as far as it will go. This is to ensure that the scan head or tip do not shadow the surface during the reaction. Then, the cooling water for the gas cracker is

turned on, as is the high voltage on the power supply. The current on the filament in the gas cracker is turned up slowly, over 5-10 min, to a final power of 40 W, which requires a current on the filament of about 2.67 A. The power is allowed to stabilize for a couple minutes, but the current is then turned down to 2 A (close to 0 W) before the gas is turned on.

The gas flow through the gas cracker and into the chamber is controlled via a leak valve. The valve is quickly opened until the pressure read on the ion gauge in the imaging chamber reads 5.0×10^{-8} torr. (The ion gauges are calibrated for nitrogen, and hydrogen has a sensitivity factor of about two relative to nitrogen, so the actual pressure in the chamber is approximately 1.0×10^{-7} torr.) Once this has stabilized for a few seconds, the power on the gas cracker is increased again to 40 W. The pressure read on the ion gauge usually decreases a few percent at this point, so the leak valve is adjusted so that the pressure again reads 5.0×10^{-8} torr. Finally, once the pressure and power have stabilized, the shutter in front of the gas cracker is opened, so that the reaction begins. At this point, the timer is started for the appropriate interval.

Once the allotted time has elapsed, the shutter on the gas cracker is shut to stop the reaction, the leak valve is closed completely, and the current on the filament in the gas cracker is turned all the way off, all within about 30 seconds. The cooling water on the gas cracker is allowed to flow for an additional minute, before it too is turned off. At this point, the scan head is lowered back onto the sample, the tip is approached onto the sample, and imaging is resumed again. The imaging usually shows a small amount of thermal drift immediately after the reaction, but this quiets down within a few minutes. When measuring the sample temperature with a thermocouple during the reactions at temperatures colder than room temperature, the surface temperature never rises more than about 1 °C, even with long exposures.

2.5 Imaging Methodology

The images used for the data analysis are STM images 512 × 512 pixels, 300 nm × 300 nm, and of good enough quality to see grain boundaries and sharp edges on domains, so that the relative areas of different phases can be measured with some accuracy. To that end, the imaging procedure is directed towards attaining images with those characteristics. The imaging conditions that I discuss below are general ranges and approximate conditions, which are varied day-by-day, and depending on the specific characteristics of the STM tip and the sample at the moment, in order to attain the highest-quality images possible. Most of this fine-tuning is through trial-and-error, looking to empirically see how the images change as the conditions are varied or the tips conditioned, without a theoretical basis for preferring one set of conditions over another.

The STM tips are 90:10 platinum-iridium (Pt/Ir) wire, with a diameter of 0.25 mm. There are two different methods of creating the atomically-sharp end of the tip that are used interchangeably within this thesis, both capable of taking images of good quality, without a strong preference for one over the other.

The first method is through cutting the tip with a pair of Lindstrom wire cutters, at a sharp angle, while applying a pulling force, creating a roughly triangular end on the tip. Tips created in this way do not tend to look as uniform and sharp under optical magnification as tips created via the second method (explained below), though they can still make quite good tips for imaging. It is only the very end of the tip on a nanometer scale that is relevant for how the tip performs while imaging.

The second method for creating an STM tip is via electrochemical etching. A piece of the Pt/Ir wire, about 1 cm long, is mounted into an electrochemical cell. A strip of nickel ribbon acts as the counter electrode, and the electrolytic solution is 2M NaCl, prepared in deionized water to minimize possible interference from other ions. A variable AC transformer (Variac) is used to run the electrochemical cell. Initially, around 3-5 mm of the Pt/Ir wire is inserted into the electrolytic solution, and about 5 V at 60 Hz AC is applied for about 30 seconds, to help clean the outside of the wire. The power is then turned off and the Pt/Ir wire adjusted so 2 mm is in the solution. The Variac is then turned up to about 35 V, and the power is turned on, etching the wire. The Variac is allowed to run until the Pt/Ir wire is etched up out of the solution, at which point the etching stops on its own. The power is turned off, and the tip is removed and rinsed with ultrapure water from a Barnstead Nanopure water purification system. The new tip is allowed to dry in air before being mounted into a tip transfer puck to be inserted into the instrument.

Once a tip is in the instrument and the sample is ready to be imaged, the STM head is lowered onto the ramp of the sample puck, and told to approach relatively quickly, using two cameras in order to monitor the distance from the tip to the sample. Once the tip is close, the STM is told to auto-approach. During the auto-approach, the derivative gain is set high, about 7 on, and the time constant is set fairly low, about 0.2, and with a low current set point of around 10 pA. A bias of +0.7 V is applied to the sample.

Once approached, the derivative gain is turned down to around 0.5-1, and imaging is started typically at a 500 nm × 500 nm scale. The scan speed is typically 300-500 ms per line, meaning that an entire image, with 512 lines, both forward and backward, takes about 5-9 min.

Imaging is typically done with a positive bias on the sample of 0.5-1 V, meaning that electrons are tunneling from the tip to the sample, imaging the empty electronic states on the surface. SAMs can be images with a negative bias on the sample, though we found that a positive bias tends to give better images.

An image is taken at 500 nm in order to get an idea of what different parts of the surface look like, before the 300-nm images are taken that will be used for data analysis. For the 300-nm images to be the most data-rich, it is preferable that they contain large, flat terraces that can be analyzed, rather than many closely-spaced atomic steps. While initially taking the 500 nm image, the lateral offsets are moved and the topography observed in the image line to find relatively flat areas. After moving the offset knobs, the image takes 1-2 min to stop drifting due to hysteresis in the piezo tube, but settles fairly quickly.

Once the 500-nm image has been taken and the topography of the surrounding area is known, one or more 300-nm images are taken, which will be used for data analysis. Often when taking the 300-nm image, the scan speed may be sped up modestly while still retaining good image quality, typically between 200-300 ms per line, meaning that it takes from about 4-5 min per image.

For each timepoint during a reaction, at least two images at 300 nm are taken of sufficient quality for analysis, in at least two different macroscopic locations on the surface. In order to move locations, the tip is retracted about 100 steps, and then moved laterally at least several hundred microns, before reapproaching and taking more images. In some but not all cases, images smaller than 300 nm will also be taken, in order to better evaluate both the tip and the sample. The close-packed hexagonal lattice of the SAM can usually start to be seen at 30-50 nm,

and the lattice spacing is used to calibrate the lateral dimensions of the STM images. The striped pattern of the lying-down phases usually start to become visible at much larger scales, often in the 300 nm images that are used for data analysis.

When imaging sample pucks that contained two samples (as for the experiments described in **Chapter 3**), several 300 nm images of acceptable quality were first obtained from one of the two samples, and then the tip was retracted quite far, and moved over to the second sample, where several images were also taken there. At the edge of the sample, it was common for a small amount of the gold to be peeling up off of the mica, making an obstacle for the tip to pass over. Therefore, the scan head was retracted nearly all the way up the ramp before moving the tip between samples, to ensure there was enough vertical clearance.

The initial imaging with a given tip onto a given sample is often not of the quality needed for data analysis, so a considerable amount of time is expended in changing imaging conditions, as well as conditioning the tip, in order to attain the required quality of images. This takes a variety of forms. In terms of imaging conditions, the sample bias and current setpoint can be varied, as can both the integral and derivative gains on the feedback loop that maintains the current setpoint. The tip speed during imaging can also be varied: if it is too high, the feedback loop cannot keep up and features begin to get streaked and blurred.

It is very necessary to condition the tip, especially after the sample has begun to be reacted with hydrogen. Some of the thiol molecules that react with atomic hydrogen apparently do not leave the sample completely, but rather lay on the surface where they may pollute the STM tip as it scans over them. Alternatively, some of the reacted thiol molecules that do leave the surface during the hydrogen atom exposure may collide with the raised tip and stick there. In

either case, it is sometimes very clear that the tip was polluted, because there is a tip change, either from consciously conditioning the tip, or randomly, and when the area is imaged again, a large mass is seen on the surface that was not there previously (see **Figure 2.4**).

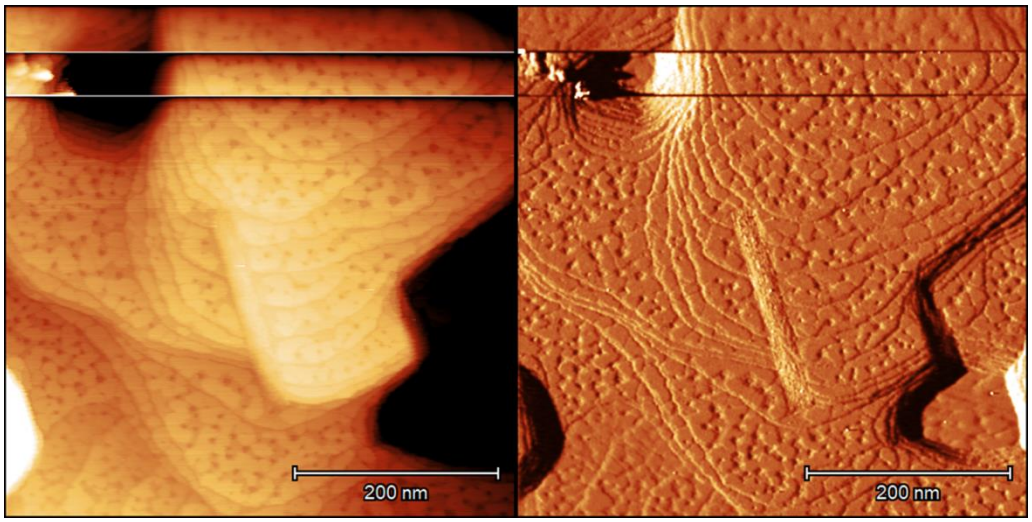

[Figure 2.4] Topographic (left) and current (right) images of decanethiol showing a tip change during scanning. The fast scan direction is from left to right, with the slow scan from top to bottom. A tip change is seen near the top, where the image becomes clearer, and material formerly on the tip is seen deposited on the surface. STM imaging conditions were 0.7V, 10 pA.

There are several means to condition the tip and induce tip changes, with different levels of perturbation to the tip. Sometimes, increasing the imaging speed to a very fast rate (<50 ms/line) for a few seconds is enough to induce a change. From there, the next step is doing a voltage pulse on the tip, applying a relatively high voltage to the sample (several volts) while the tip is in tunneling range, for a short amount of time. The high field induced at the tip may remove pollutants from the tip and even rearrange the metal molecules near the tip. A weak form of this voltage pulse can be attained by switching the bias voltage from positive to negative and then back, and then progressively stronger pulses can be applied through the software, with

either positive or negative bias on the sample. Finally, the most drastic way to change the tip is to deliberately crash it into the surface, which can change the geometry of the tip, as well as transfer material between the probe and the surface. Crashing the tip seems to work relatively well on samples with a gold surface (such as SAMs), but less well on non-metallic surfaces, such as graphite. We hypothesize that this is due to the transfer of some gold from the surface to the tip, where it forms a clean metal layer to interact with the sample.

2.6 Data Preparation and Analysis

All of the image processing presented in this thesis was carried out using Gwyddion, a free scanning probe microscopy image analysis program.[56] The results were stored in a spreadsheet, which was also used to do the math for averaging different values at each timepoint and estimating error bars. Finally, the data was plotted using MATLAB, which was also used to add the lines for our modeled behavior and extract rate constants from the model.

The basic scheme for analyzing the images taken during the course of a reaction with atomic hydrogen is presented in **Figure 2.5**. In brief, each terrace of the image is analyzed independently. A terrace is flattened, and a mask is applied to isolate it. A height threshold is applied, so that etch pits and reacted areas (which are topographically lower) are masked, while the remaining standing-up phase is not. The area of the standing up phase is then compared to the area of the entire terrace.

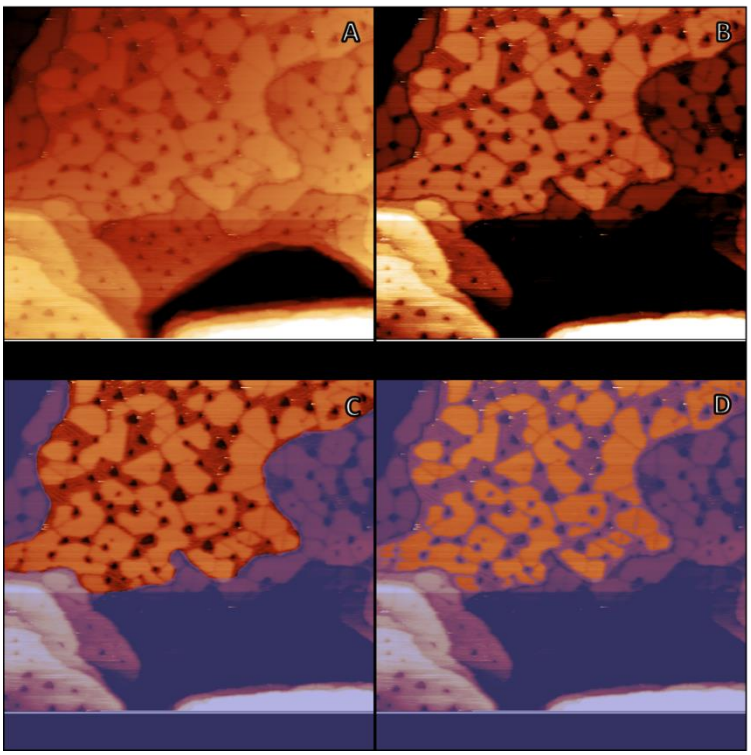

[Figure 2.5] This series of images show the procedure used to find the area percentage of standing up phase. The original image (**A**) is tilted to obtain a flat terrace (**B**), followed by masking off that terrace and measuring the total area (**C**), and finally using a height threshold to measure only the area of the standing phase (**D**).

This process is repeated independently for each terrace, giving a range of ratios at each timepoint during the reaction. We've simplified this by taking an average weighted by the area of each terrace (to minimize the small sample size effects that tend to occur more frequently on small terraces). To estimate the uncertainty in each timepoint, the standard deviation of all of the terraces from all images was used.

Some care must be taken in the image analysis, as we were only measuring the fraction of the area that was standing-up phase, not the fraction that was reacted. Even before the SAMs had been exposed to any atomic hydrogen, only around 90% of the surface was recorded as being the standing-up phase. This is due to the gold vacancy islands, or etch pits, that are on the

surface, and which get caught by the height threshold. To account for this effect, all of the graphs were normalized to the initial value for the ratio of standing-up phase.

There was a significant amount of variability in the total amount of time taken to react, when the reaction of the same type of SAM was carried out on different days. To account for this, the room temperature reactions for the experiments described in **Chapter 3** were run two at a time: with each chain length paired with a 1-decanethiolate SAM. When all four chain lengths were worked up and presented on the same graph, the time-points of each pair that were reacted together were multiplied by a constant, such that all of the 10-carbon reactions overlapped, giving accurate relative reactivities of all four chain lengths.

To create the histogram shown in **Figure 3.9**, representative images were used of SAMs composed of each of the 4 chain lengths, both from before exposure to hydrogen, and from images where around 50% of the standing-up phase remains (the exact images used are shown in **Figures A.3.9a-d**). For each image, the etch pits are masked one at a time, drawing freehand in Gwyddion, and the total mask area measured, giving the area of each etch pit on the image. The histogram is made in Microsoft Excel, using bin sizes of 20 nm^2.

2.7 Model Building

The model that we currently use to describe the reaction of alkanethiolate SAMs with atomic hydrogen is described in **Section 3.3**. I will not be expanding further here on what that model is, or how we arrived at it. Rather, I would like to briefly describe how the model used to generate the curves plotted on **Figures 3.6** and **4.4**, and how the parameters were chosen to model the data.

Once the initial form of the differential equation was decided for the model (see **equation 3.1**), it was integrated to give a closed form for the proportion of standing up phase as a function of time (see **equation 3.2**, reproduced below as **equation 2.1**).

$$\theta = \frac{k_2\theta_{max}}{k_2 - k_1} - A\mathrm{e}^{(k_2 - k_1)t} \tag{2.1}$$

This equation has three parameters, θ_{max}, k_1 and k_2. The first, θ_{max} is a physical quantity of the system, the initial proportion of the surface that is measured to be standing-up phase (essentially all of the surface except for domain boundaries and etch pits). It is estimated directly based on the initial datapoints for each reaction. The two rate constants are not directly coming from the data, but instead are fit. The length-independent constant, k_2 should be the same for all 4 chain lengths according to our model, and being much larger than k_1 should dominate the shape of the curve, so a compromise k_2 value was chosen to give a reasonable curve shape for all 4 chain lengths. From that point, k_1 was chosen for each curve to best follow the actual data.

The data as well as the modeled curves were all generated in MATLAB, and the rate constants were tweaked until the modeled curves overlayed the plotted data. No mathematical fitting was done, and with so many parameters, there is significant risk of overfitting and considerable uncertainty. For this reason, we are not comfortable putting too much stock in the exact values found, and rather prefer to look at the overall trend.

Chapter 3: Chain-Length Dependent Reactivity of Alkanethiolate Self-Assembled Monolayers with Atomic Hydrogen

3.1 Introduction

Thiolate self-assembled monolayers (SAMs) on Au(111) are some of the most well-studied systems in the surface science community.[25,26,57,58] These materials consist of densely-packed organic molecules, chemisorbed onto a metal substrate and arranged in a highly ordered 2D polycrystalline structure. The tunability of the molecules' chemical functionality allows for the control of surface properties such as wetting[59–62], adhesion[61,63], photoactivity[64], and chemical reactivity[26]. This versatility has enabled SAMs to be used in a variety of applications ranging from biomimetics[59,63,65,66] to corrosion inhibition.[67,68]

SAMs have also proven to be of great importance in the study of gas-surface interactions, where their tunability allows one to study reaction dynamics as a function of individual surface parameters such as chain length, odd- or evenness, or chemical functionality.[12] They have been used as model surfaces to gain insight on the reactivity of atomic gases with hydrocarbons[12], which has importance in applications such as passivating electronic surfaces with organic thin films.[11,69]

Previous studies have shown[12,18–21,70,71] that atomic hydrogen reacts with alkanethiolate SAMs on Au(111), resulting in their removal from the surface. Gorham et al.[12] used X-ray photoelectron spectroscopy (XPS) to study the impact of chain length on the rate of removal. They found that for short ($C \leq 12$) alkanethiolate SAMs, the sulfur is hydrogenated and the molecules are removed entirely from the surface. Conversely, long chain SAMs react more slowly and are removed in fragments *via* chemical erosion of the hydrocarbon film. The Kandel

group later studied the reaction of 1-octanethiolate SAMs with hydrogen using ultra-high vacuum scanning tunneling microscopy (UHV-STM).[18–21,71] This direct imaging technique yielded a greater understanding of the mechanistic details of the reaction, such as the formation of gold adatom islands and the influence of local surface environment on the rate of monolayer erosion.

Building on these studies, we present a detailed analysis of the effect of chain length on the reaction of alkanethiolate SAMs with atomic hydrogen, using UHV-STM to investigate the evolution of the surface on the microscopic scale. *In situ* imaging was used to track the reaction progression of a series of SAMs (8-11 carbons long) by monitoring the relative areas of high- and low-density phase SAM on the surface after exposure to hydrogen. Based on these experimental data, we propose an exponential model that describes the observed kinetics. Restructuring of the substrate over the course of the reaction was also examined, and it was determined that shorter chain SAMs cause greater rearrangement of the underlying gold surface.

3.2 Experimental Details

Experiments were performed in a UHV chamber (base pressure of 1×10^{-10} Torr) that houses both an RHK 350 Beetle UHV-STM/AFM and a Mantis MGC-75 thermal gas cracker. This *in situ* dosing setup has the gas cracker oriented 50^{o} from the imaging stage's surface normal and located 80 mm from the sample. Gas exposure from the cracker is controlled by a manual shutter. Atomic hydrogen was produced by passing molecular hydrogen (backing pressure of 1×10^{-7} Torr) through the gas cracker's heated iridium capillary. Under these conditions, a cracking efficiency of approximately 90% can be expected.[72] A hydrogen flux on

the order of 10^{12} H atoms cm^{-2} s^{-1} was determined for our experimental setup. Sample exposures were performed for intervals of 3-15 min, during which the microscope scan head was retracted several inches to prevent the tip from shadowing the surface.

n-Alkanethiolate SAMs were prepared on flame-annealed Au(111)-on-mica substrates from Keysight Technologies using solution-deposition methods. The substrates were immersed in 1.0 mM solutions of 1-octanethiol (8C), 1-nonanethiol (9C), 1-decanethiol (10C) and 1-undecanethiol (11C) in ethanol for 2.5 h at 60 ^{o}C. Samples were rinsed with ethanol and dried in air prior to placement in the UHV chamber. STM images were taken with a bias voltage of 0.70 V and a tunneling current set point of 10 pA. In order to obtain reliable relative reaction rates between different experiments, two 2.5 mm × 5 mm samples were mounted together and dosed simultaneously for each reaction: a 1-decanethiol sample, to be used as a reference between the different experiments, and a second SAM sample of desired length (8-, 9- or 11-carbons long). All STM image processing was performed using Gwyddion, an open-source software for SPM data analysis.[56]

3.3 Results and Discussion

Figure 3.1 shows a representative set of STM images for the progression of a sample's reaction; in this case, decanethiolate. Similar sets of images for the octanethiolate, nonanethiolate and undecanethiolate samples can be found in **Figures 3.2-3.4**. The zero-minute panel shows the SAM prior to atomic hydrogen exposure, and illustrates the typical features of an alkanethiolate SAM on Au(111).

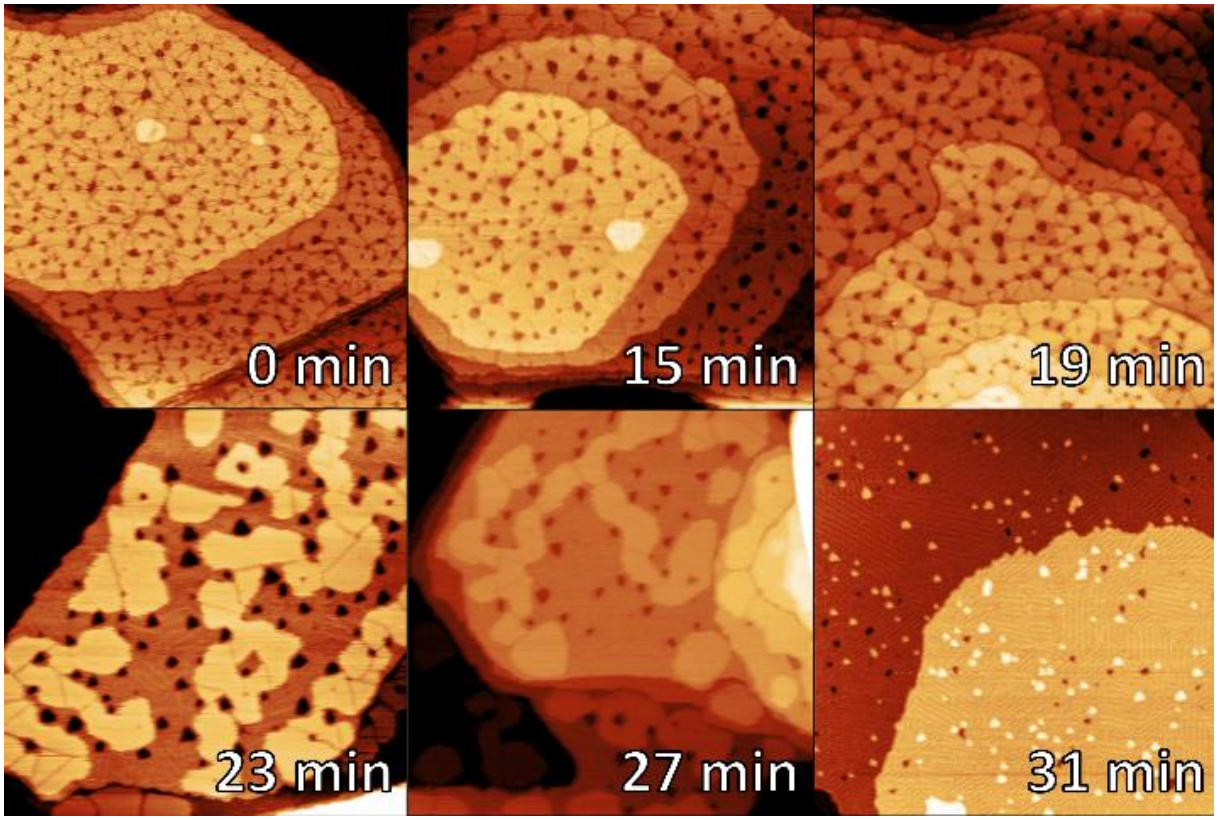

[Figure 3.1] A succession of STM images of a 1-decanethiol SAM at various time points during its exposure to atomic hydrogen. The erosion of standing-up phase becomes apparent after dosing for ~19 min, visible as the thickening of grain boundaries and topographically lower regions. All images are 300 nm × 300 nm, STM imaging conditions were 0.7 V, 10 pA.

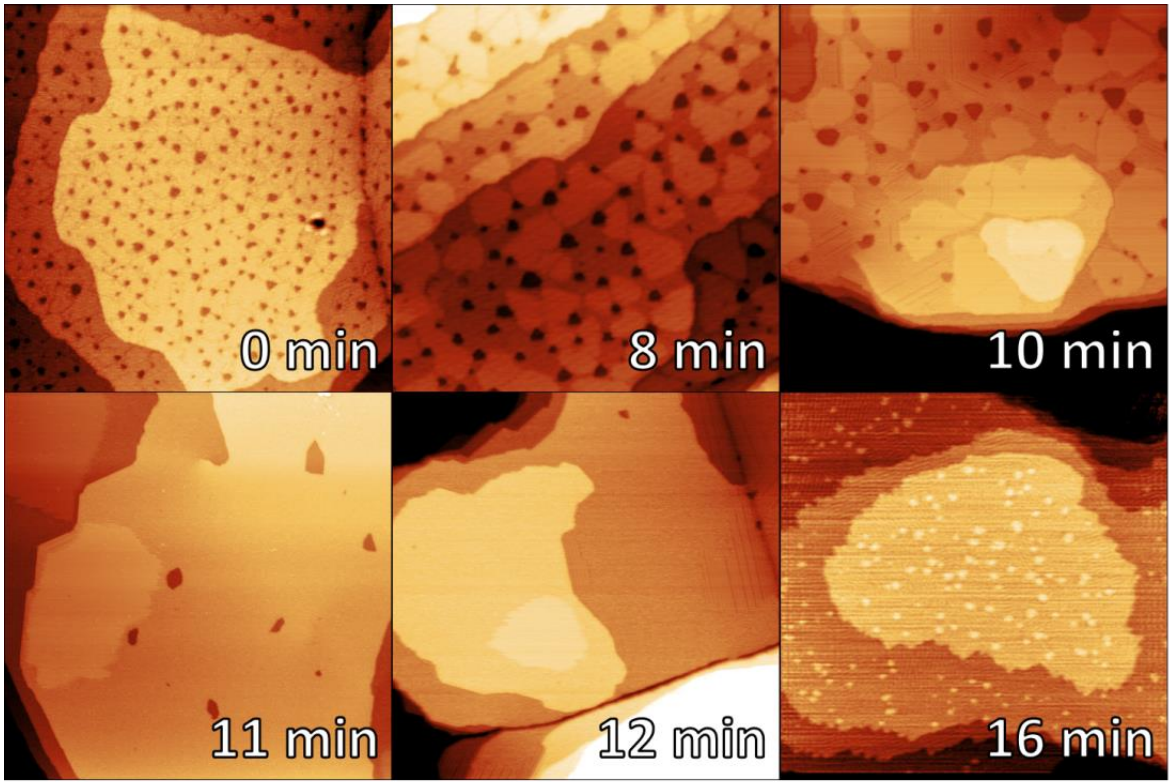

[Figure 3.2] A succession of STM images of a 1-octanethiol SAM at various time points during its exposure to atomic hydrogen. The erosion of standing-up phase was already quite apparent when the first time point was taken after 8 minutes. All images are 300 nm × 300 nm, STM imaging conditions were 0.7 V, 10 pA.

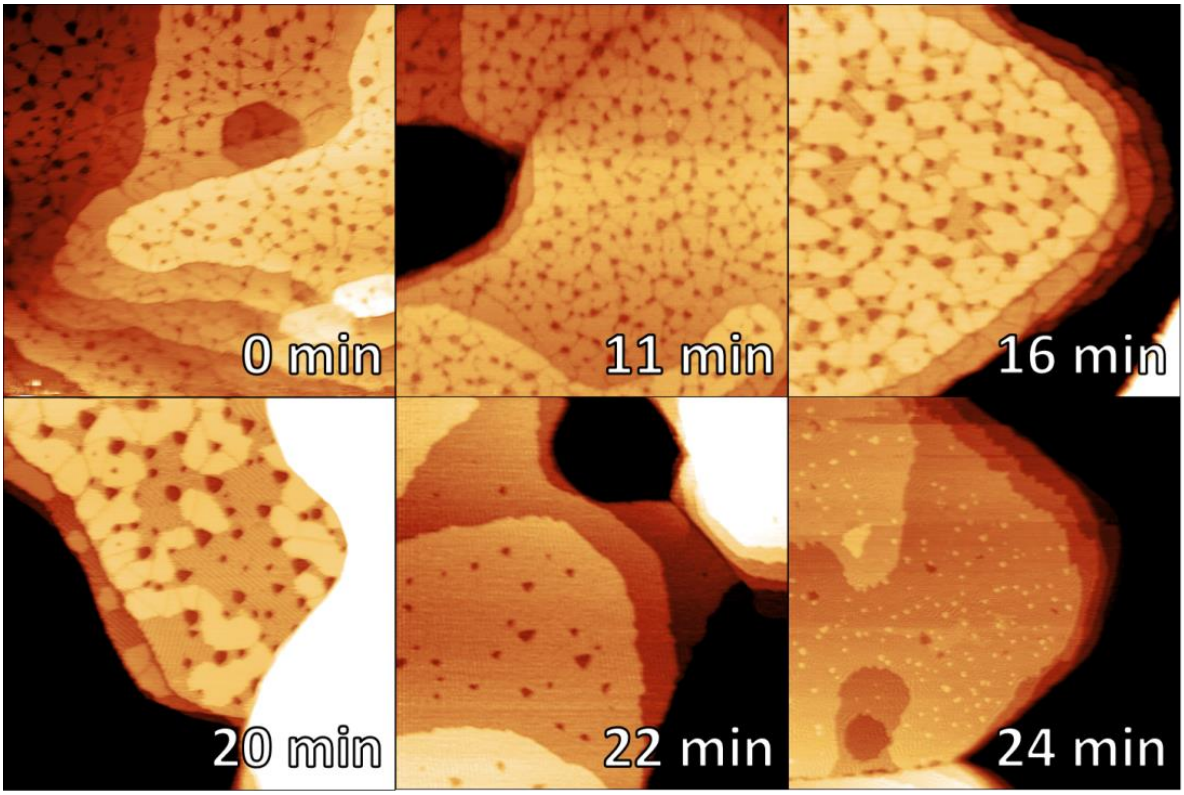

[Figure 3.3] A succession of STM images of a 1-nonanethiol SAM at various time points during its exposure to atomic hydrogen. The erosion of standing-up phase becomes apparent after dosing for ~16 min, visible as the thickening of grain boundaries and topographically lower regions All images are 300 nm × 300 nm, STM imaging conditions were 0.7 V, 10 pA.

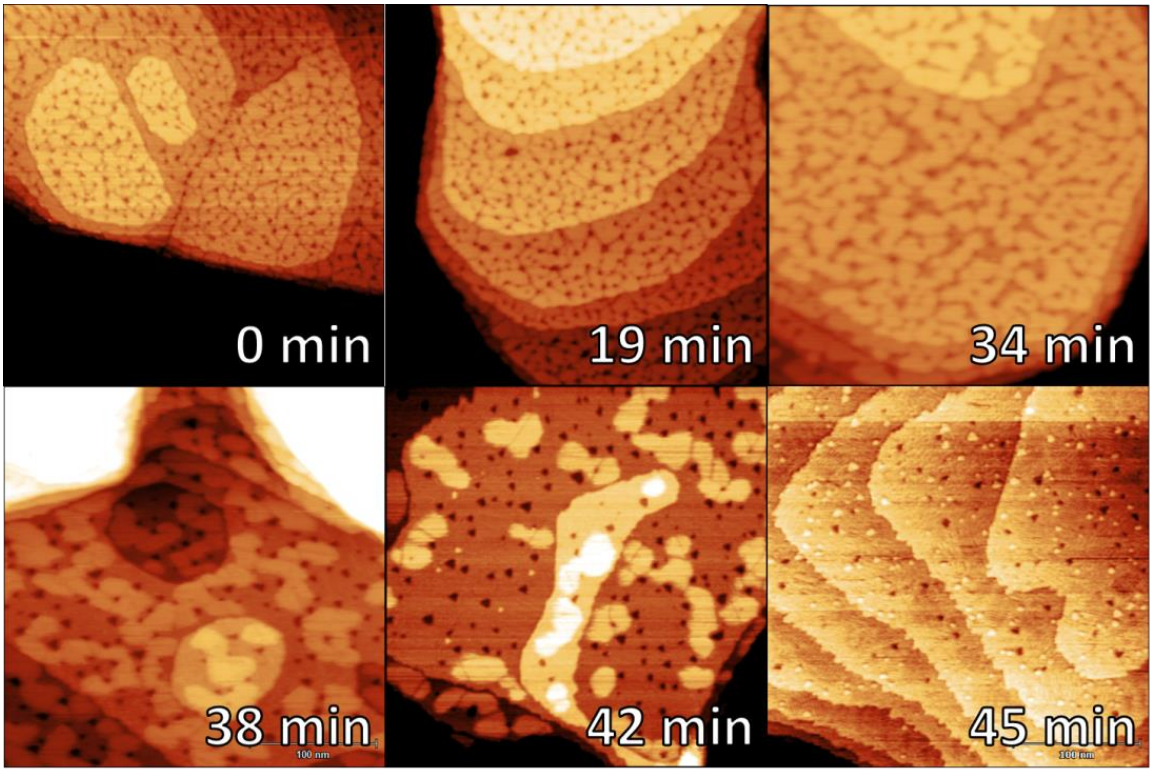

[Figure 3.4] A succession of STM images of a 1-undecanethiol SAM at various time points during its exposure to atomic hydrogen. The erosion of standing-up phase starts to be come visible after dosing for ~19 min, visible as the thickening of grain boundaries and topographically lower regions All images are 300 nm × 300 nm, STM imaging conditions were 0.7 V, 10 pA.

The thiol molecules self-organize into a standing-up, hexagonal close-packed structure, with a lattice constant of 0.50 nm and a c(4×2)R30^{o} superlattice (**Figure 3.5**). The alkane tails are in an all-*trans* configuration tilted 32^{o} from the surface normal, and three degenerate rotational orientations are possible due to the symmetry of the underlying gold lattice.[26,27] Domains of standing-up phase have a diameter of approximately 20-30 nm and are separated by grain boundaries where molecules of different orientations meet. Gold vacancy islands, also known as etch pits, appear during the formation of the SAM and are spread across the surface

between domains. These defects are typically circular, with a diameter around 5 nm, and are filled with standing-up phase SAM **(Figure 3.5 C)**.

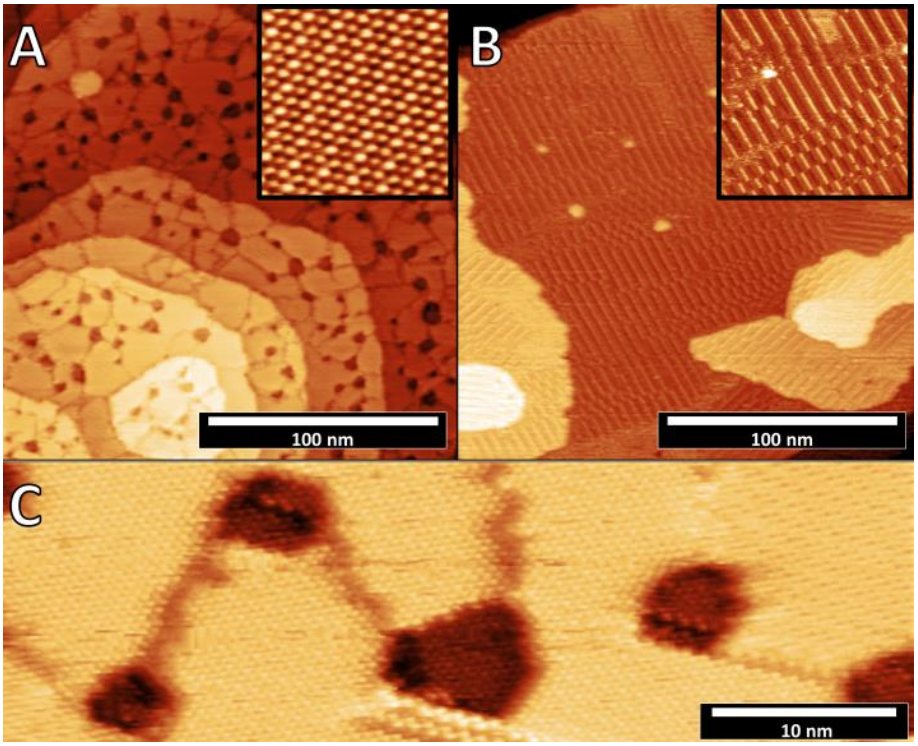

[Figure 3.5] (A) STM image of 1-decanethiol SAM composed entirely of hexagonally close-packed standing-up domains. Inset (7 nm × 7 nm) shows atomic resolution and the c(4×2) superlattice. **(B)** Ordered low density lying-down phases of 1-decanethiol (inset 50 nm × 50 nm). **(C)** Image showing standing-up phase inside the gold vacancy islands. STM imaging conditions were 0.7 V, 10 pA.

Previous studies have shown[18,19] that the gold atoms taken from the etch pits are incorporated into the alkanethiolate monolayer, with a ratio of two thiol molecules per gold adatom. The later panels of **Figure 3.1** show the general progression of the SAM upon reaction with hydrogen. Initial reactivity is evidenced by the thickening of the grain boundaries, as molecules are removed from the surface and remaining thiolates begin to form lower density phases. These include various ordered lying-down phases, which are observed as bright and dark

stripes on the surface (**Figure 3.5 B**).[28,29] Upon further exposure to hydrogen, the lower density areas expand and interconnect, leaving isolated pools of standing-up phase. Eventually, no standing-up phase remains on the surface and small gold islands are observed, formed from the adatoms previously incorporated in the SAM.[18,19] For this experiment, the reaction is considered complete when no standing-up phase remains on the surface.

When hydrogen travels through the organic layer of pristine standing-up phases, it is possible that the tilt angle relative to the gas cracker plays a role in the reactivity. The alkane tails are tilted ~32° from the surface normal, while the gas cracker is 50° from the surface normal. The geometry of the sample, scan head, and gas cracker provides a direct line of sight from the gas cracker to the sample, whether the scan head is retracted as in these experiments, or lowered onto the sample. The gas cracker is 8.0 cm away from the sample, which is about 0.5 cm × 0.5 cm, a solid angle of 0.004 sr, meaning all atomic hydrogen comes to the sample from the same direction, which is known relative to the imaging direction. The azimuthal angle of the alkane tails in some domains point more towards the direction of the gas cracker, so the atomic H encounters different geometries in the alkane layer that may make it more or less likely to react with certain domains. However, the STM does not provide information on the azimuthal angle of the alkanethiolate tails, so it is not known if the hydrogen is preferentially reacting with domains of a certain character, and differences in the reactivity between domains were not obvious, making it impossible to draw definitive conclusion as to any differences in reactivity based on the orientation of the alkane tails of the standing phase to the gas cracker from the current experiment.

To quantify the reaction, **Figure 3.6** presents the normalized area fraction of standing-up phase on the surface (θ/θ_{max}) as a function of time exposed to hydrogen flux (t). In order to obtain relative rates between all four chain lengths, the exposure times for each reaction pair (10C and nC, where n = 8, 9, 11) were adjusted such that all three decanethiolate reaction times overlapped. A control experiment in which two 10C samples were dosed simultaneously was performed to verify that both samples received the same exposure to hydrogen, and variations in the Au(111) surface structure did not significantly impact the reactivity. As shown by the graph, the rate of SAM reaction with atomic hydrogen decreases with increasing chain length.

There was no noticeable variance in reactivity based on the odd-/evenness of the chains; in all cases, an increase in chain length by one carbon atom caused a proportional increase in reaction time. The orientation of the terminal methyl group of an alkanethiolate SAM varies based on the parity: alkanethiolate SAMs with an even number of carbon atoms have a terminal methyl group oriented nearly vertically, ~26° from the surface normal, while those with an odd number of carbons per molecule are oriented more horizontally, ~53° from the surface normal[73,74]. This has been seen to influence some physical properties such as the wetting and friction forces[75–78], and therefore plausible that a difference in reactivity would be seen. However, such an effect was not observed.

Exponentially modelled curves have also been superimposed on the experimental data. All four chain lengths exhibit similar kinetic behavior, as indicated by the comparable shapes of the curves; the reactions all begin slowly, but their rates increase as the amount of standing-up phase decreases.

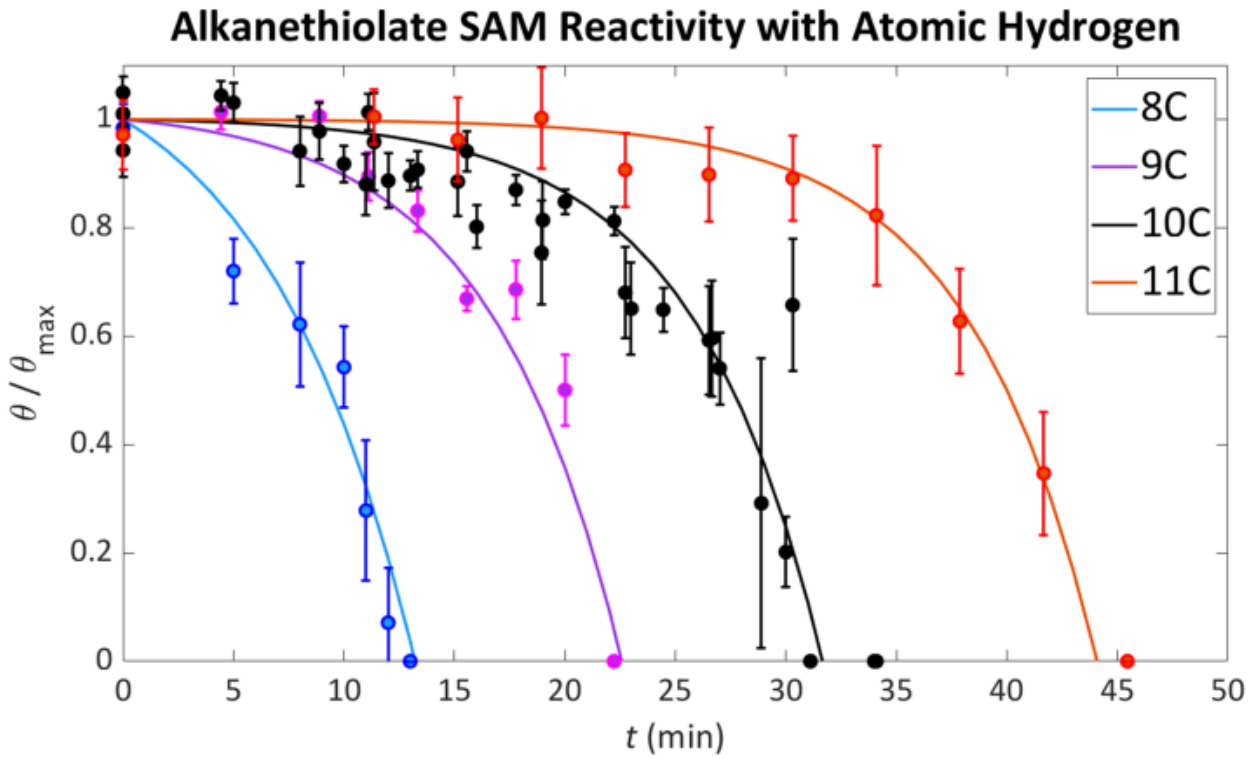

[Figure 3.6] Plot of the experimental reaction progression of 8C, 9C, 10C and 11C SAMs with atomic hydrogen on Au(111). Each data point is a weighted average of measurements from several locations on the sample. The error bars correspond to 1σ of the θ values calculated for each time point. The exposure times have been adjusted with multiplicative factors so that all of the 10C curves overlap, and the coverage has been normalized to exclude the initial etch pits and not-standing areas. The model exponential curves are based on two different rates: the length-independent constant, k_2 is 0.17 min^{-1}, and the length-dependent constant k_1 is 0.0001 min^{-1}, 0.0008 min^{-1}, 0.0040 min^{-1}, and 0.0250 min^{-1} for 11C, 10C, 9C, and 8C, respectively.

The trends seen in the experimental data of **Figure 3.6** suggest that the SAMs' reactivity with hydrogen increases as thiolates are removed and the amount of standing-up area on the surface decreases. This implies that low-density thiolate phases react more readily than the close-packed standing-up phase, in agreement with previous studies that showed greater reactivity at defected sites such as grain boundaries and eroded areas.[21] A model was therefore generated to describe the area fraction of standing-up phase on the surface (θ) as a function of time exposed to hydrogen flux (t) based on two rate constants (k_1 and k_2). The first constant, k_1, defines the rate at

which hydrogen reacts with standing-up phase, while k_2 defines the rate of reaction with low-density phases. The differential equation describing this behavior can be written as

$$-\frac{d\theta}{dt} = k_1\theta + k_2(\theta_{max} - \theta) \tag{3.1}$$

where θ_{max} is the surface fraction of standing-up phase at $t = 0$. Note that both θ and θ_{max} exclude the standing-up phase contained in etch pits, for analysis simplicity. Equation 1 therefore integrates to

$$\theta = \frac{\theta_{max}}{1-\left({}^{k_1}/_{k_2}\right)} - A\mathrm{e}^{(k_2-k_1)t} \tag{3.2}$$

For the constant of integration A, when we assume $\theta(t=0) = \theta_{max}$ (the coverage of standing-up phase is monotonically decreasing), we find

$$A = \frac{1}{\left({}^{k_2}/_{k_1}\right)-1} \tag{3.3}$$

When reacting with the standing-up phase, atomic hydrogen must pass through the tightly-packed alkane tails in order to reach the reactive sulfur at the surface. Longer chains produce both a thicker and more highly-ordered layer, thereby hindering the hydrogen's progress. This implies that k_1 should be strongly and inversely dependent on alkanethiolate chain length. However, the thickness of low-density SAM phases is independent of chain length, suggesting that these areas will react uniformly for all four samples. In this model, k_2 was therefore required to be the same for each chain length.

Equation 2 with a k_2 of 0.17 min^{-1} and k_1 values ranging from 0.0001 min^{-1} to 0.0250 min^{-1} produces exponential curves that are in good agreement with the experimental data (**Figure 3.6**). These values conform to the expectation that the low-density phases are much more reactive than the pristine close-packed domains ($k_2 \gg k_1$). Furthermore, the length-dependent rate constants decrease in value exponentially for each additional carbon on the alkane chain. This suggests that small increases in chain length cause disproportionately large decreases in the standing-up phase's permeability to hydrogen. However, once the surface has begun reacting, further reactivity primarily occurs in low-density regions and all four SAMs exhibit similar kinetics.

A major advantage of using STM for this study is that the reactions can be explored on a molecular level, rather than being restricted to statistical averages. **Figure 3.7** shows visual comparisons of all four types of SAM, both before and after exposure to atomic hydrogen. Prior to reaction, the size and density of domains and etch pits are similar across all four samples. However, differences in etch pit size and distribution become evident in the 8C and 9C samples after exposure. For these shorter chain substrates, the etch pits grow larger, become more triangular in shape, and decrease in density across the surface. On the other hand, the etch pits of 10C and 11C samples do not exhibit any major changes throughout the reaction.

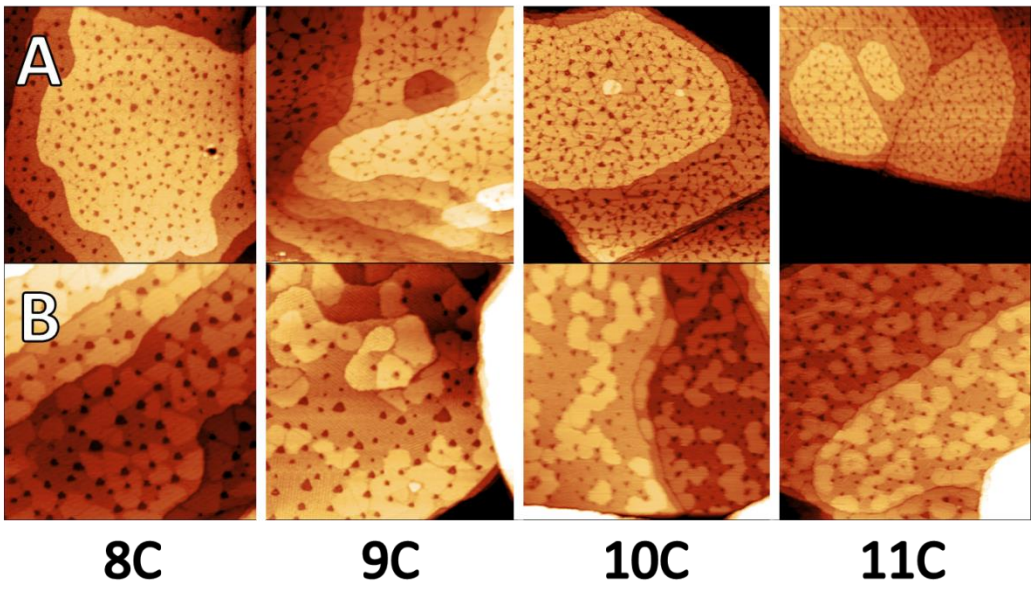

[Figure 3.7] Representative 300 nm × 300 nm images of each of the four SAMs (8C, 9C, 10C, and 11C) **(A)** prior to reaction and **(B)** with 50% standing-up phase coverage remaining. Changes in surface morphology, particularly etch pit size and shape, are apparent in the 8C and 9C samples following hydrogen exposure.

Distributions of etch pit sizes for each chain length are displayed in **Figure 3.9**. A noticeable shift is apparent in the 8C and 9C histograms, indicating an increase in mean etch pit area upon reaction. The 10C and 11C histograms, however, remain largely unchanged.

Previous work by Poirier investigated etch pit restructuring on low-density 1-butanethiolate monolayers and found that the etch pits annealed *via* Oswald ripening.[22,30] This process is observed upon the creation of low-density phases during the reaction of alkanethiolates with hydrogen, as seen in **Figure 3.8**. The extent to which etch pits ripen is strongly dependent on chain length: 8C shows the largest amount of rearrangement, followed by 9C, and little rearrangement is observed in the 10C and 11C samples. This is explained by the

stronger intermolecular forces between the long-chain SAM molecules, leading to reduced mobility of the thiols and their corresponding gold adatoms across the surface.

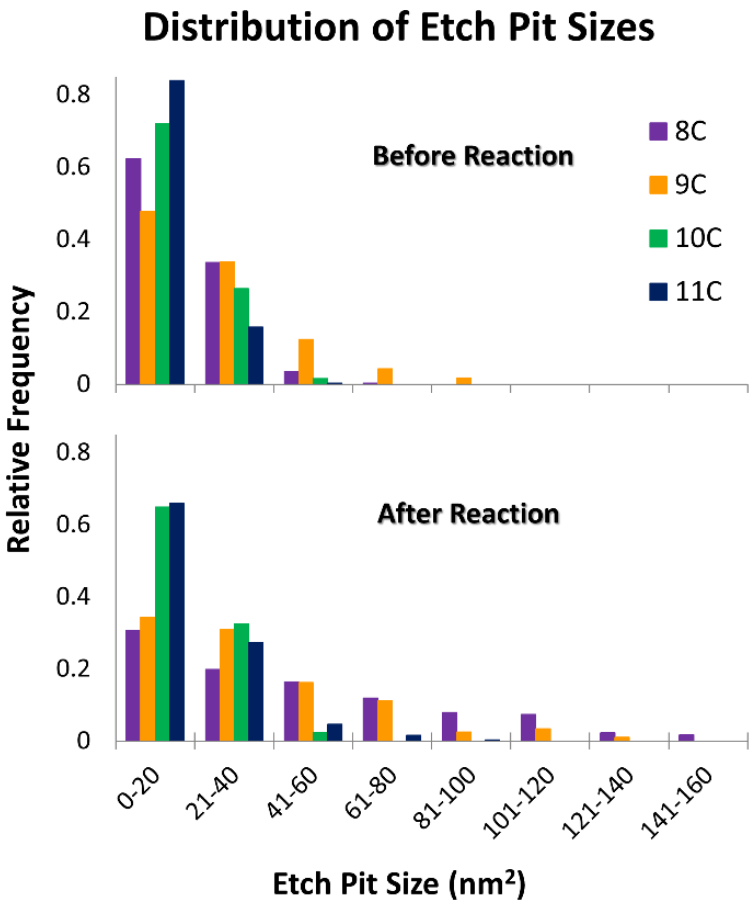

[Figure 3.8] Histograms of etch pit areas for all four chain lengths prior to atomic hydrogen exposure (*top*) and with 50% standing-up phase coverage remaining (*bottom*). Shorter chain length SAMs show a greater growth in mean etch pit area, with increases of 33 nm^2, 12 nm^2, 2 nm^2, and 5 nm^2 for 8C, 9C, 10C and 11C respectively.

3.4 Conclusions

We have successfully used the direct-imaging capabilities of STM to study the effect of temperature on the spatiotemporal evolution of alkanethiolate SAMs reacting with atomic hydrogen. It was found that small decreases in film thickness lead to disproportionately large increases in reaction rate. The trends in the experimental data demonstrate that previously

reacted areas of the surface are more susceptible to hydrogen attack than standing-up phase domains. This lead to the exponential modelling of the data with two rates: one for hydrogen reacting with standing-up phase, which is dependent on SAM chain length (k_1 ranging from 0.0001 min^{-1} to 0.0250 min^{-1}), and one for low-density phase reactions, which is the same for all samples (k_2 = 0.17 min^{-1}).

In addition to quantifying the relative rates of reaction of the alkanethiolate SAM series, STM allowed for the tracking of changes in surface morphology throughout the reaction. Notable changes occurred in the size, shape, and density of the samples' etch pits over the course of hydrogen exposure. This was attributed to Oswald Ripening, with the growth of certain etch pits at the expense of others, and was seen to have a dependence on chain length. Few changes were observed in the 10C and 11C samples, while there was significant growth in mean etch pit area for the 8C and 9C SAMs. The weaker intermolecular forces between the shorter-chain molecules permit greater mobility of the thiols and their corresponding gold adatoms, allowing for more extensive surface rearrangement.

This STM study has provided a detailed analysis of the effect of chain length on the reaction rate and surface evolution of alkanethiolate SAMs upon exposure to atomic hydrogen. Experiments designed to elucidate the mechanism of this reaction are underway, using cryogenic cooling to limit the mobility of thiol molecules on the surface. The first of these experiments is detailed in the next chapter.

Chapter 4: Temperature-Dependent Reactivity of Alkanethiolate Self-Assembled Monolayers with Atomic Hydrogen

4.1 Introduction

As discussed in the introduction of **Chapter 3**, self-assembled monolayers (SAMs) are an extremely well-studied system for investigating a variety of properties of organic surfaces where it is desired to have a well-ordered and well-characterized surface. The properties of alkanethiolate SAMs are tunable by changing the organic group of the thiols used in making the SAMs. The organic functional groups can be changed to vary the reactivity, wetting, or photoactivity. The thickness of the organic layers can be varied by changing the chain lengths of the organic groups.

In the previous chapter, we used the tunibility of SAMs to investigate the effect that the layer thickness had on their reactivity with hydrogen. We found that the chain length had a large effect on the rate of reactivity, with slightly longer chains creating a disproportionately large decrease in reactivity.

In this chapter, we describe an experiment testing the effect of temperature on the reactivity of decanethiolate SAMs with atomic hydrogen. Atomic hydrogen reacts with decanethiolate SAMs by traveling through the alkane layer and reacting with the sulfur-carbon bond at the surface.[12] Therefore, cooling the SAM may make it harder for the hydrogen atoms to reach the surface by decreasing the thermal motion and forming more well-ordered domains. Additionally, our model proposed in **Section 3.3** relies on the alkanethiolate molecules on the surface being able to move readily during the course of the reaction, so that as some of the alkanethiolate molecules are removed and the density decreases, the remaining molecules can

relax into the less-dense lying down phases. Our model assumes the lying-down phases react more readily, due to hydrogen not having to traverse the alkane layer present in standing-up phase (and also react at roughly the same speed, independent of chain length). However, at cold enough temperature the movement of alkanethiolate molecules on the surface will slow to a point that there is no significant rearrangement, and the mechanism of reaction should change markedly. STM is able to image surfaces on a molecular scale, and so changes in reactivity can be seen not only in the rates of reactivity, but also the morphology of the surface during the course of the reaction.

4.2 Experimental Details

The experiments in this chapter are carried out with the same experimental setup as described in **Section 3.2**. An RHK 350 UHV-STM/AFM is used for imaging, while the reaction with atomic hydrogen is carried out with a Mantis MGC-75 thermal gas cracker pointed at the sample stage.

Decanethiolate SAMs were prepared on flame-annealed Au(111)-on-mica substrates from Keysight Technologies using solution-deposition methods, as described in **Section 3.2**. STM images were taken with a bias voltage of 0.70 V and a tunneling current set point of 10 pA. In contrast to the experiments described in **Chapter 3**, all of the samples for these experiments were mounted individually, with only one type of SAM per run. All STM image processing was performed using Gwyddion, an open-source software for SPM data analysis.[34] Our exposure graph and Arrhenius plot were created with Matlab.

Reactions of decanethiolate SAMs with atomic hydrogen were carried out with the SAM held at 3 different temperatures: room temperature (around 295 K), 270K, and 250K. For the reactions at depressed temperatures, the sample was cooled with liquid nitrogen in a flow cryostat thermally connected to the sample stage. The liquid nitrogen on its own will cool the sample to around 110 K, colder than we wished to conduct most of the reactions with.. A filament underneath the sample is then heated in order to heat the sample from 110 K to the experimental temperature. The filament power is controlled with a Lakeshore 331 Temperature Controller, using a thermocouple on the sample as input for a proportional-integral (PI) control loop controlling the filament current. One sample was exposed to decanethiolate at 110 K for a total of 135 minutes, and then imaged both at 110 K and after being warmed to room temperature.

4.3 Results and Discussion

Figure 4.1 shows a representative set of STM images for the progression of a sample's reaction at room temperature. The zero-minute panel shows the SAM prior to atomic hydrogen exposure, and illustrates the typical features of an alkanethiolate SAM on Au(111), as describe in **Section 3.3.**

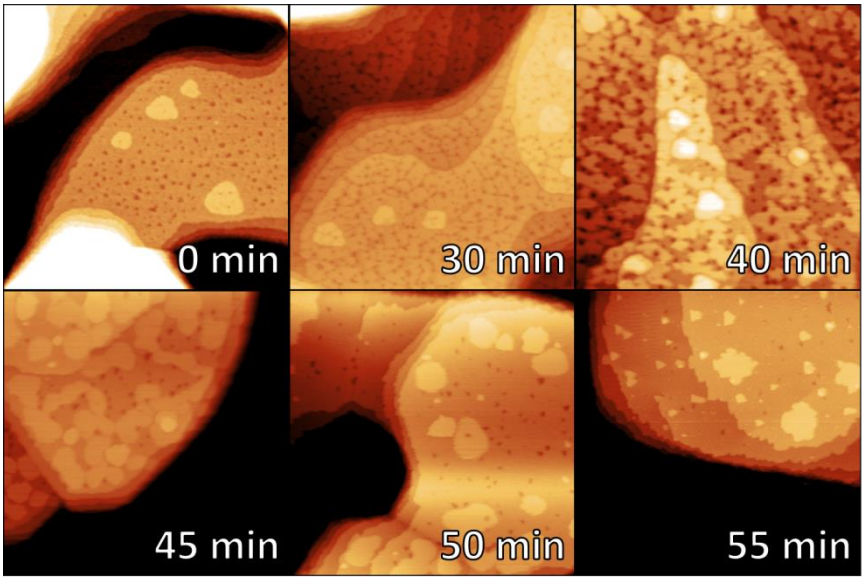

[Figure 4.1] A succession of STM images of a 1-decanethiol SAM at various time points during its exposure to atomic hydrogen at room temperature (295 K). This is the same type of reactivity as seen in all SAMs in chapter 3. All images are 300 nm × 300 nm, STM imaging conditions were 0.7 V, 10 pA.

The reaction at 270 K (**Figure 4.2**) shows a similar progression to the reaction at room temperature, though at a considerably slower rate. At this colder temperature, the reaction takes about twice as long to reach completion.

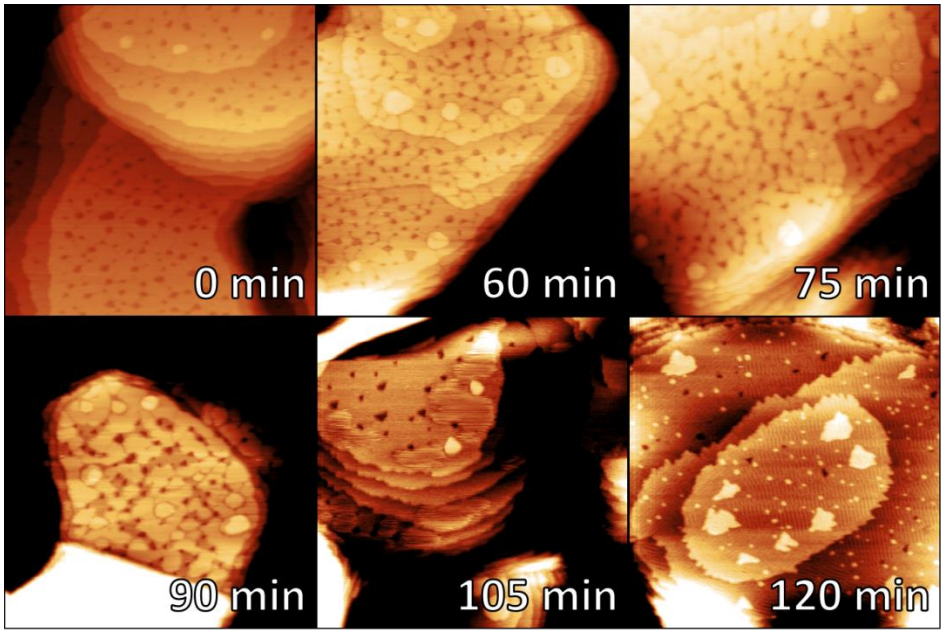

[Figure 4.2] A succession of STM images of a 1-decanethiol SAM at various time points during its exposure to atomic hydrogen at 270 K. This is the same type of reactivity as seen in all SAMs in chapter 3. All images are 300 nm × 300 nm, STM imaging conditions were 0.7 V, 10 pA.

In contrast to the hydrogen exposures at 295 K and 270 K, the reaction at 250 K exhibits different morphology as the reaction progresses (**Figure 4.3**). The very initial stages of the reaction appear the same, though further delayed: the grain boundaries start to widen and areas near etch pits start to erode after around 90 minutes. However, once the size of the eroded areas reach a certain size, small raised spots appear in the reacted area. As the reaction continues, the standing-up domains continue to erode with the small spots filling in the reacted area.

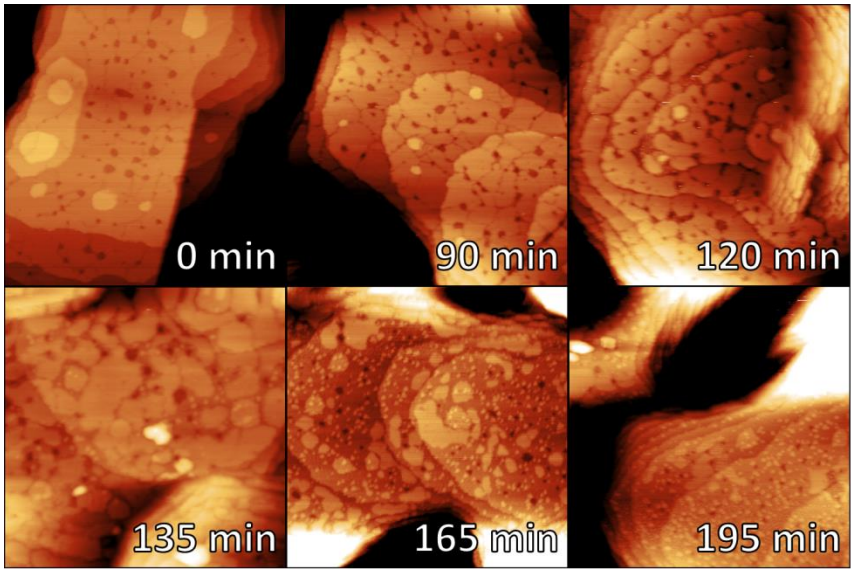

[Figure 4.3] A succession of STM images of a 1-decanethiol SAM at various time points during its exposure to atomic hydrogen at 250 K. The progression of the reaction has changed, with small gold islands appearing much earlier, while standing-up domains still exist in large numbers on the surface. All images are 300 nm × 300 nm, STM imaging conditions were 0.7 V, 10 pA.

The difference between the reaction at 250 K as opposed to reactions at warmer temperatures can be seen further when the proportion of remaining standing-up phase is plotted for each of the reactions against time (**Figure 4.4**). The curves of the reactions at 295 K and 270 K are the same general shape as each other and of all of the different chain length alkanethiols from **Chapter 3**. The curve of the reaction at 250 K, on the other hand, has a different shape. It begins similarly, with a long time period with little visible reaction, followed by an increasing rate of reaction as the surface begins to react. However, rather than the rate of reaction continuing to increase throughout the entire experiment, an inflection point occurs when somewhere around 20% of the standing up phase remains, and the rate of reactivity decreases sharply, and it takes a significant amount of time to remove the last of the standing-up phase.

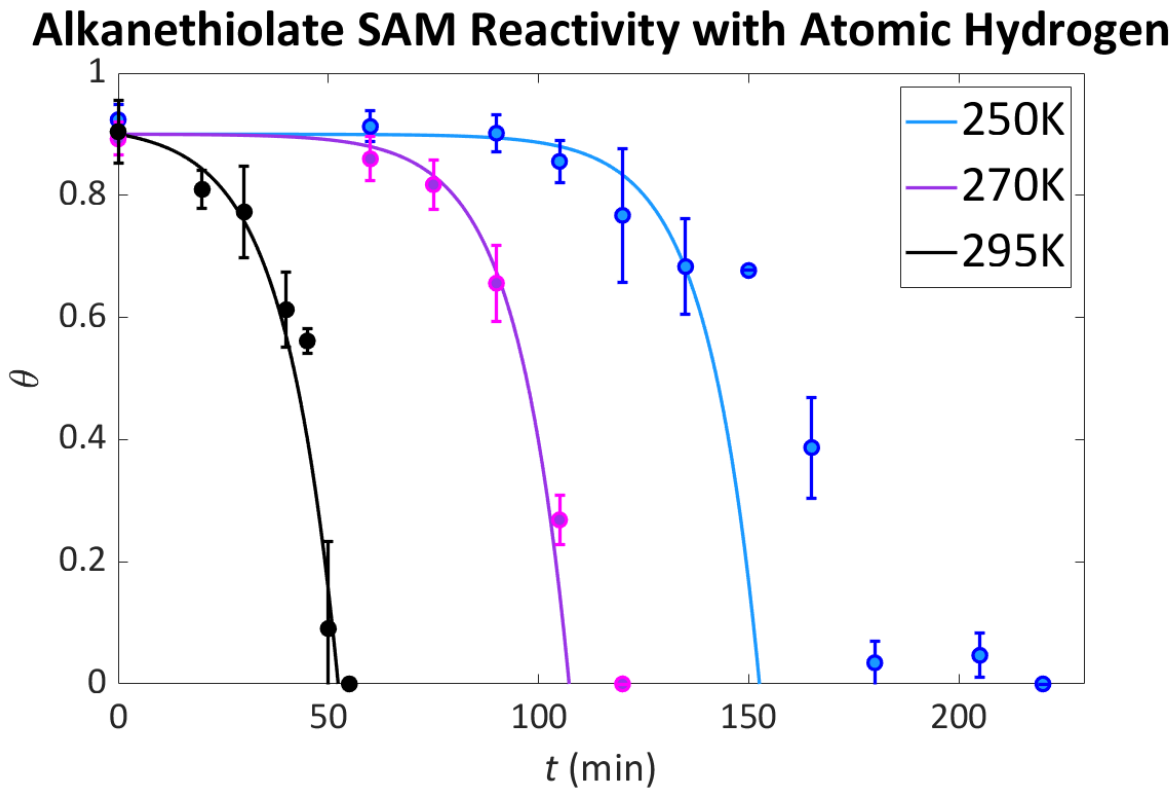

[Figure 4.4] Plot of the experimental reaction progression of decanethiol SAMs at three different temperatures with atomic hydrogen on Au(111). Each data point is a weighted average of measurements from several locations on the sample. The error bars correspond to 1σ of the θ values calculated for each time point. The model exponential curves are based on two different rates: the temperature-independent constant, k_2 is 0.08 min^{-1}, and the length-dependent constant k_1 is 4×10^{-6} min^{-1}, 15×10^{-6} min^{-1}, and 1300×10^{-6} min^{-1} for 250K, 270K, and 295K, respectively.

The reason for this shift is likely due to the mobility of the alkanethiolate molecules on the gold surface during the course of the reaction. At room temperature, it is known that thiolates bonded to the surface can move and rearrange into lower-energy configurations as some of them are removed. This means that as the reaction begins and areas without standing-up phase appear, some of the remaining molecules in the standing-up phase relax into lying-down phases in the newly cleared area. It is this property, we believe, that results in the shape of the reaction curves during the later part of the exposure at 270 K and 295 K. The model assumes

that lying-down molecules react much more easily with hydrogen than standing-up phase, as the hydrogen does not need to make it through unreactive alkane tails to reach the sulfur group. For this reason, as the fraction of the area not standing up increases, the rate of reaction increases through the entire reaction.

At 250 K, it appears that the molecules do not substantially move during the course of the reaction. No new molecules come from the remaining standing-up phase to fill the reacted areas, so the gold adatoms that were incorporated into those areas remain in the area and form gold islands. This also explains the different shape of the graph for the last phases of reactivity. The remaining standing-up phase does not spread over reacted area, so as the fraction of the standing-up phase is reduced, the hydrogen is less likely to hit a phase of standing-up phase, and the reactivity decreases in the very latter stages.

The initial stages of the reaction at 250 K do look similar to the warmer reactions. Presumably, the initial stages of the reaction, dominated by reaction of atomic hydrogen with the decanethiolate standing phases, is not much affected by the diffusion (or lack thereof) of the thiolate molecules across the surface. The reaction speed does initially accelerate in the 250 K reaction, perhaps indicating an increase in defected areas near grain boundaries and etch pits, where hydrogen has an easier time reaching the surface and reacting with the gold, even if the thiolate molecules do not lie down and form striped low-density phases.

In additionion decanethiolate SAM to atomic hydrogen at 110 K for 135 minutes, long enough that we would have seen a reaction at any of the warmer temperatures from this experiment. No reaction is observed at those temperatures, even after the sample was warmed back up to room temperature. There was a possibility that the alkanethiolate molecules were still

getting hydrogenated at that temperature, but that the alkanethiol molecules remained physically absorbed to the surface. The fact that the exposed surface did not change upon warming to room temperature suggests that this is not the case, and that the very cold temperature does indeed drastically suppress the reaction of atomic hydrogen with alkanethiolate SAMs.

The same model of reactivity as in **Chapter 3** was used, except with a temperature dependent and independent constants instead of chain length dependent and independent. This equation is show in **Equation 4.1**, where k_2 is the temperature independent rate, corresponding to reaction with lying down phases, and k_1 the temperature dependent rate, corresponding to reaction with standing phases.

$$\theta = \frac{\theta_{max}}{1-\left({}^{k_1(T)}/_{k_2}\right)} - Ae^{(k_2-k_1(T))t} \qquad (4.1)$$

Three curves were placed onto the graph in **Figure 4.4**. The model does not work for the late stages of the reaction at 250 K, so a best guess for parameters was made to fit the curve to the earlier stages of the reaction. There will consequently be greater error in the fitting of the 250 K rates (if indeed the model is at all valid even in the early stages of that reaction). An Arrhenius plot of the temperature-dependent rate constants is shown in **Figure 4.5.**

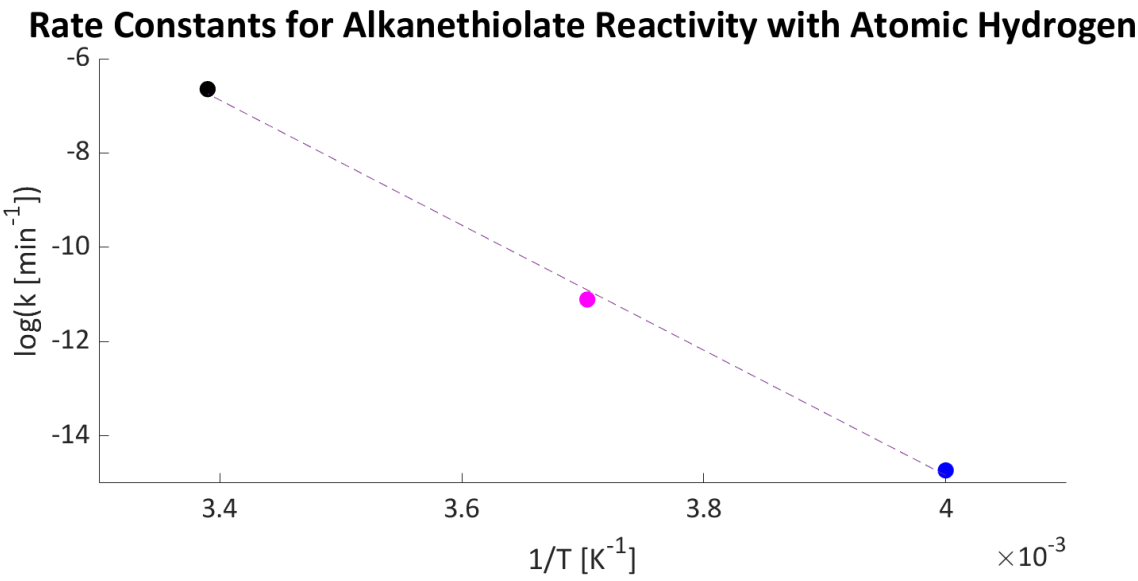

[Figure 4.5] Arrhenius plot of the temperature-dependent rate constant. The extracted activation energy is about 110 kJ/mole

The exact values have considerable uncertainty: the modeled curves have two parameters to fit with only 3 datasets, leading to a strong possibility of overfitting (especially considering that the model breaks down at 250 K). Additionally, the values for the temperature-dependent rate constant are heavily dependent on the value chosen for the temperature-independent rate constant, and only at 295 K and 270 K do we believe that the mode of reaction represented by that rate constant is present. There is also no guarantee that the rate of reaction with lying-down phases is indeed independent of temperature, as we have assumed. We do believe that the rate limiting step is the hydrogen penetrating the alkane tails of the standing-up phase, while hydrogen should react with an exposed sulfur atom with comparatively high speed, justifying this assumption, but do not have the data to fully support it at this time. Doing an additional reaction at a temperature where the original mechanism should hold, such as 305 K, would give more insight into the validity of this model for the reaction of atomic hydrogen with

decanethiolate SAMs at different temperatures. Keeping in mind these caveats, the Arrhenius plot shows an activation energy for the temperature-dependent rate of around 110 kJ/mole. This corresponds to the energy barrier for the hydrogen to diffuse through the alkane tail layer to reach the surface.

4.4 Conclusions

We have successfully used the direct-imaging capabilities of STM to study the effect of temperature on the evolution of alkanethiolate SAMs reacting with atomic hydrogen. It was found that rate of reaction decreased with decreasing temperatures. We fit the data with an exponential model with two rates: one for hydrogen reacting with standing-up phase, which is dependent on SAM chain length (k_1 ranging from 4×10^{-6} min^{-1} to 1300×10^{-6} min^{-1}), and one for low-density phase reactions, which is the same for both the room temperature and 270 K reactions ($k_2 = 0.08$ min^{-1}).

Additionally, the course of the reaction at 250 K changed considerably. Instead of the rate exponentially increasing as the reaction progressed, an inflection point occurred and it took a very long amount of time to remove the last 20% or so of the standing phase. Additionally, small gold islands began appearing much earlier in the reaction, leading us to conclude that the alkanethiolate molecules on the surface do not appreciably move on the surface at 250 K, while they do at 270 K and warmer temperatures.

This STM study has provided a preliminary analysis of the effect of chain length on the reaction rate and surface evolution of alkanethiolate SAMs upon exposure to atomic hydrogen, especially with respect to the faster reaction with lying down phase. Experiments designed to

investigate further the reaction with standing phase are underway, by investigating how decreases in temperature affect the rate of reaction of different chain-length alkanethiolates.

Appendix 1: Transfer of alkanethiols between samples during reaction with atomic hydrogen and subsequent STM imaging

An interesting phenomenon was observed while running some of the experiments that are described in chapter 3. These were the reactions where two alkanethiolate SAMs with different chain-lengths were exposed at the same time to atomic hydrogen from the thermal gas cracker.

In some of the images that were taken after some amount of exposure, but before the standing-up phase was completely removed, sometimes the shorter-chain alkanethiolate SAM would show bright spots interspaced in the standing-phase areas (see figure A1.3.1). We interpreted this as being some molecules of the longer-chain alkanethiolate intermixed with the shorter chain thiolate on the sample. Intentionally prepared mixed SAMs show that such mixtures are possible.[79]

It is unknown exactly how the thiol molecules are transferred. They do not appear to transfer from one sample to the other just by sitting next to each other, or by sequential imaging of one and then the other, before any exposure to atomic hydrogen has taken place. The initial images taken before any reaction do not show this mixing. Therefore, it is probable that the action of atomic hydrogen on the SAMs is necessary for the mixing that was observed. The atomic hydrogen hydrogenates the alkanethiol, which then leave the surface. It is possible that some of the thiols within the chamber then re-deposit onto the other sample from the gas phase.

It is also possible that the thiols are being transported by the tip when moving from one sample to the other. We do know that the tip can become polluted with molecules. We occasionally see a tip change, and after imaging the same area again, a large deposit of material that came from the tip and caused the tip change when it left (See figure A1.3.1). There are a

couple ways that thiol molecules could make their way onto the tip. The tip remains several centimeters directly above the sample during exposure to atomic hydrogen, so thiols that react and enter the gas phase might impact the tip and then stick. It's also possible that some of the reacted molecules are still physisorbed on the surface, and when the tip is lowered for imaging it picks some of the molecules up.

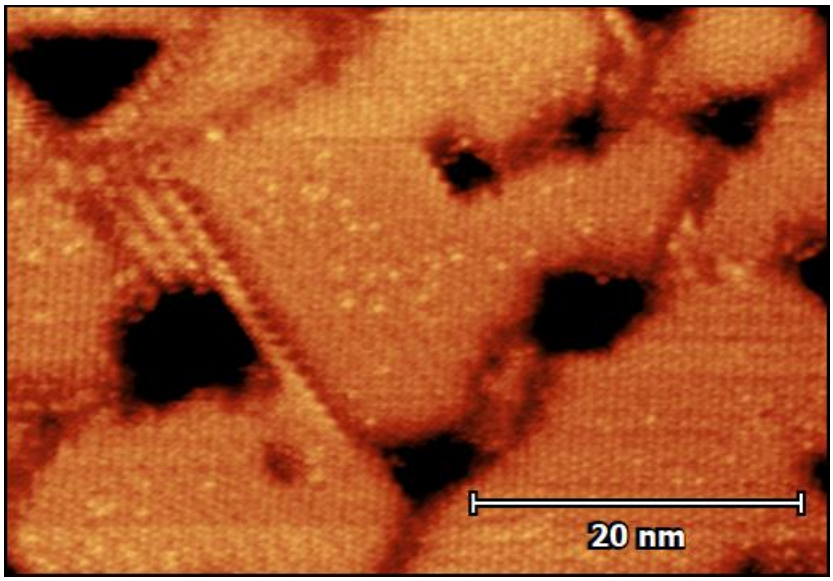

[Figure A1.1] Image showing the bright spots occurring during the reaction of 2 samples of different chain lengths. This is an image of a nonanethiol SAM which was reacted along with a decanethiol SAM, after exposure to 10 minutes of atomic hydrogen.

Appendix 2: Raw Data Referenced for Figures

This section contains images that were used in measuring reacted area for the experiments presented in this thesis, as well as the file name. These images were acquired with the RHK UHV-350 AFM/STM. All of the images used in this thesis are in an electronic repository with the Steve Sibener Group.

Figure A2.1

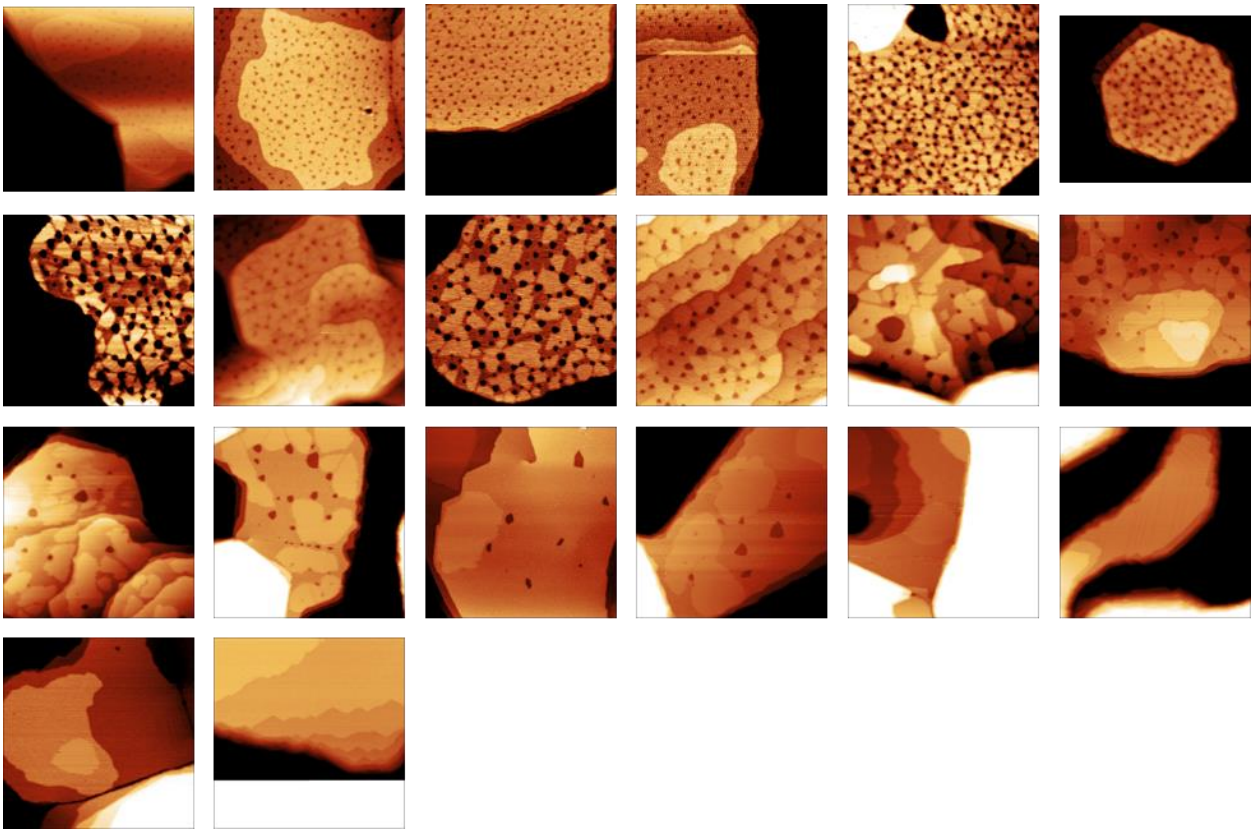

These are the images used in constructing the 8 carbon plot in **Figure 3.6**

Figure A2.1 (con)

Directory: Appendix\8_10C Run\8C

Filenames: Starting at top left, going across the rows:
2018_04_17_SplitCrystal_8C_0min0004
2018_04_17_SplitCrystal_8C_0min0010
2018_04_17_SplitCrystal_8C_0min0012
2018_04_17_SplitCrystal_8C_5min0028
2018_04_17_SplitCrystal_8C_5min0033
2018_04_17_SplitCrystal_8C_5min0036
2018_04_18_SplitCrystal_8C_5min0003
2018_04_18_SplitCrystal_8C_5min0017
2018_04_18_SplitCrystal_8C_8min0035
2018_04_18_SplitCrystal_8C_8min0038
2018_04_19_SplitCrystal_8C_8min0007
2018_04_19_SplitCrystal_8C_10min0018
2018_04_20_SplitCrystal_8C_10min0025
2018_04_20_SplitCrystal_8C_10min0029
2018_04_23_SplitCrystal_8C_11min0002
2018_04_23_SplitCrystal_8C_11min0008
2018_04_23_SplitCrystal_8C_11min0011
2018_04_23_SplitCrystal_8C_12min0035
2018_04_23_SplitCrystal_8C_12min0037
2018_04_24_SplitCrystal_8C_13min0017

Figure A2.2

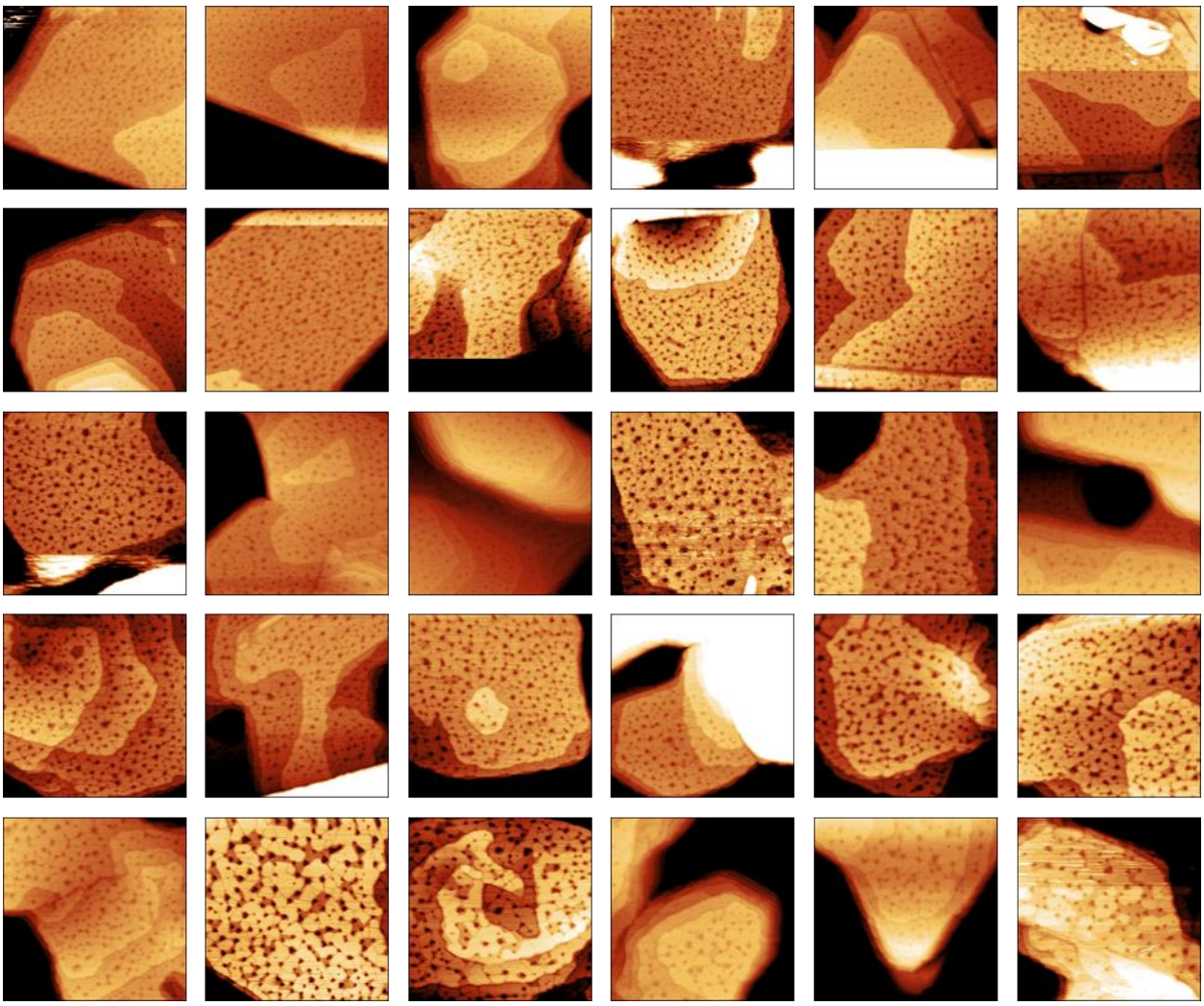

These are the first 30 images used in constructing the 10 carbon plot in **Figure 3.6** that was acquired at the same time as the 8C reaction

Figure A2.2 (con)

Directory: Appendix\8_10C Run\10C

Filenames: Starting at top left, going across the rows:
2018_04_26_SplitCrystal_10C_19min0018
2018_04_17_SplitCrystal_10C_0min0020
2018_04_17_SplitCrystal_10C_0min0022
2018_04_17_SplitCrystal_10C_0min0025
2018_04_17_SplitCrystal_10C_5min0038
2018_04_18_SplitCrystal_10C_5min0022
2018_04_18_SplitCrystal_10C_5min0027
2018_04_18_SplitCrystal_10C_8min0044
2018_04_18_SplitCrystal_10C_8min0046
2018_04_18_SplitCrystal_10C_8min0047
2018_04_19_SplitCrystal_10C_8min0001
2018_04_19_SplitCrystal_10C_8min0003
2018_04_19_SplitCrystal_10C_10min0010
2018_04_19_SplitCrystal_10C_10min0013
2018_04_19_SplitCrystal_10C_10min0015
2018_04_20_SplitCrystal_10C_10min0033
2018_04_23_SplitCrystal_10C_11min0016
2018_04_23_SplitCrystal_10C_11min0024
2018_04_23_SplitCrystal_10C_11min0026
2018_04_24_SplitCrystal_10C_12min0003
2018_04_24_SplitCrystal_10C_12min0004
2018_04_24_SplitCrystal_10C_12min0006
2018_04_24_SplitCrystal_10C_12min0007
2018_04_24_SplitCrystal_10C_13min0019
2018_04_24_SplitCrystal_10C_13min0021
2018_04_24_SplitCrystal_10C_13min0028
2018_04_26_SplitCrystal_10C_16min0001
2018_04_26_SplitCrystal_10C_16min0002
2018_04_26_SplitCrystal_10C_16min0003
2018_04_26_SplitCrystal_10C_16min0005

Figure A2.3

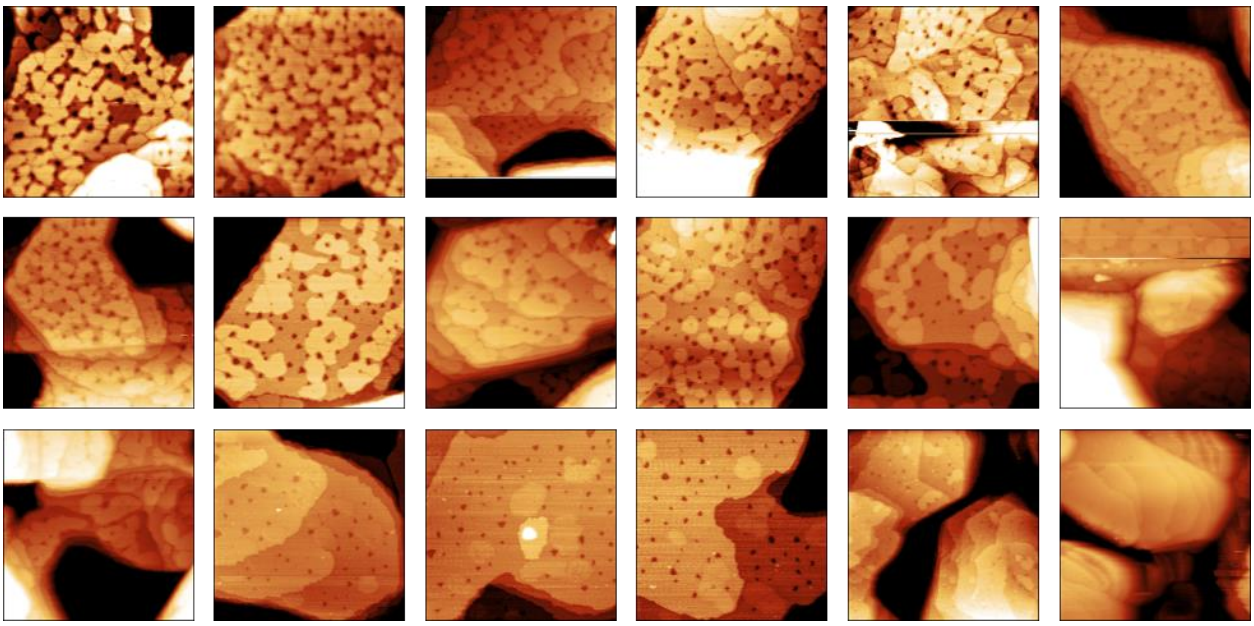

These are the final 18 images used in constructing the 10 carbon plot in **Figure 3.6** that was acquired at the same time as the 8C

Figure A2.3 (con)

Directory: Appendix\8_10C Run\10C

Filenames: Starting at top left, going across the rows:
2018_04_27_SplitCrystal_10C_19min0002
2018_04_27_SplitCrystal_10C_19min0006
2018_04_27_SplitCrystal_10C_19min0009
2018_04_30_SplitCrystal_10C_23min0003
2018_04_30_SplitCrystal_10C_23min0005
2018_04_30_SplitCrystal_10C_23min0008
2018_04_30_SplitCrystal_10C_23min0016
2018_04_30_SplitCrystal_10C_23min0019
2018_04_30_SplitCrystal_10C_23min0020
2018_04_30_SplitCrystal_10C_27min0026
2018_04_30_SplitCrystal_10C_27min0029
2018_04_30_SplitCrystal_10C_27min0030
2018_04_30_SplitCrystal_10C_27min0032
2018_05_01_SplitCrystal_10C_30min0012
2018_05_01_SplitCrystal_10C_30min0015
2018_05_01_SplitCrystal_10C_30min0017
2018_05_01_SplitCrystal_10C_34min0028
2018_05_02_SplitCrystal_10C_34min0000

Figure A2.4

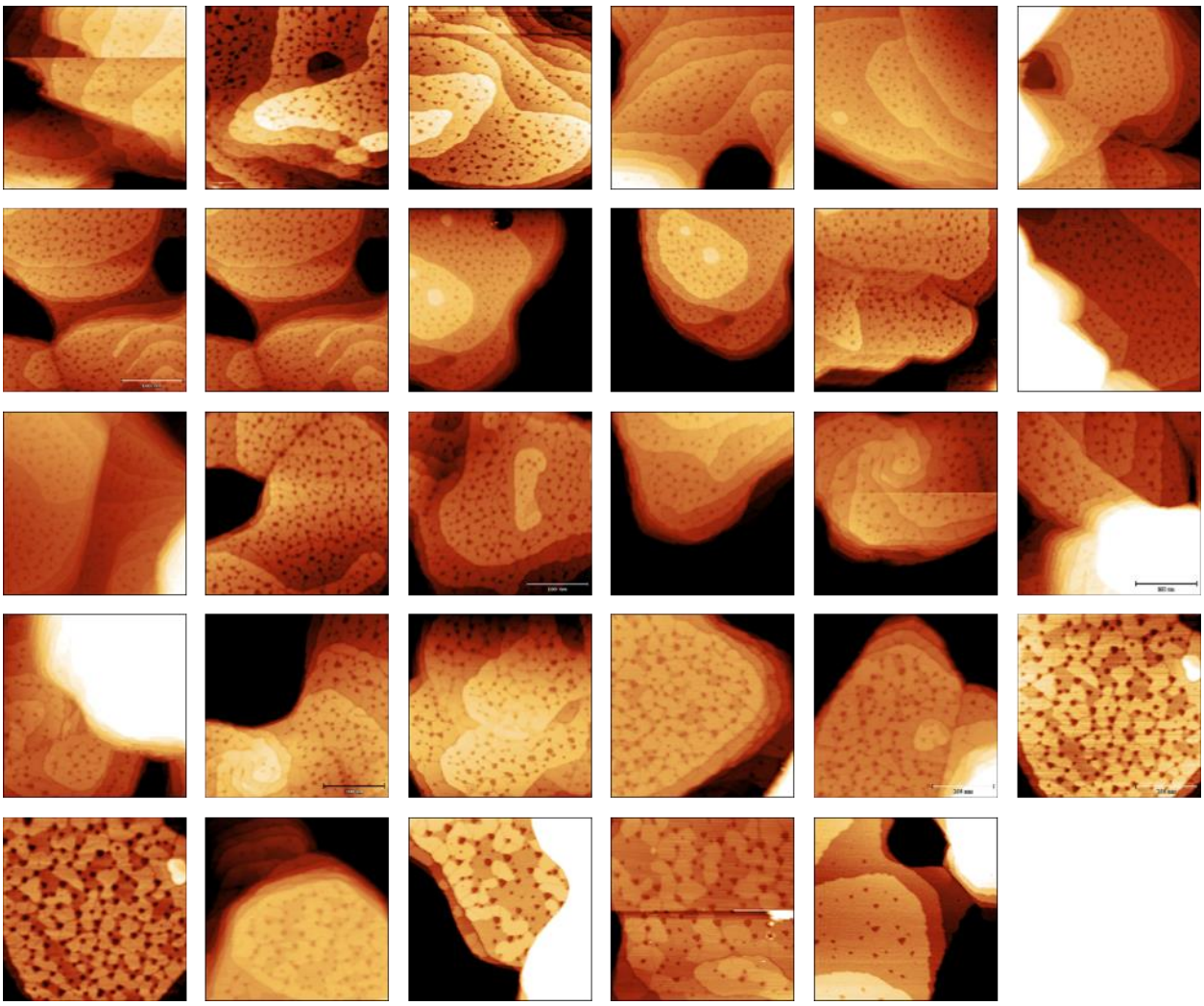

These are the images used in constructing the 9 carbon plot in **Figure 3.6**

Figure A2.4

Directory: Appendix\9_10C Run\9C

Filenames: Starting at top left, going across the rows:
2018_03_28_split_sample2_9C_unreactred0005
2018_03_28_split_sample2_9C_10min0031
2018_03_29_split_sample2_9C_10min0001
2018_03_29_split_sample2_9C_10min0003
2018_03_29_split_sample2_9C_20min0037
2018_03_29_split_sample2_9C_20min0040
2018_03_29_split_sample2_9C_20min0042
2018_03_29_split_sample2_9C_20min0042b
2018_03_29_split_sample2_9C_20min0051
2018_03_29_split_sample2_9C_20min0052
2018_03_30_split_sample2_9C_25min0014
2018_03_30_split_sample2_9C_25min0017
2018_03_30_split_sample2_9C_25min0018
2018_03_30_split_sample2_9C_25min0024
2018_04_01_split_sample2_9C_25min0005
2018_04_01_split_sample2_9C_25min0006
2018_04_01_split_sample2_9C_30min0028
2018_04_01_split_sample2_9C_30min0029
2018_04_01_split_sample2_9C_30min0030
2018_04_01_split_sample2_9C_30min0031
2018_04_02_split_sample2_9C_30min0001
2018_04_02_split_sample2_9C_35min0033
2018_04_02_split_sample2_9C_35min0034
2018_04_03_split_sample2_9C_40min0023
2018_04_03_split_sample2_9C_40min0023_final
2018_04_03_split_sample2_9C_40min0028
2018_04_03_split_sample2_9C_45min0048
2018_04_04_split_sample2_9C_45min0007
2018_04_04_split_sample2_9C_50min0010

Figure A2.5

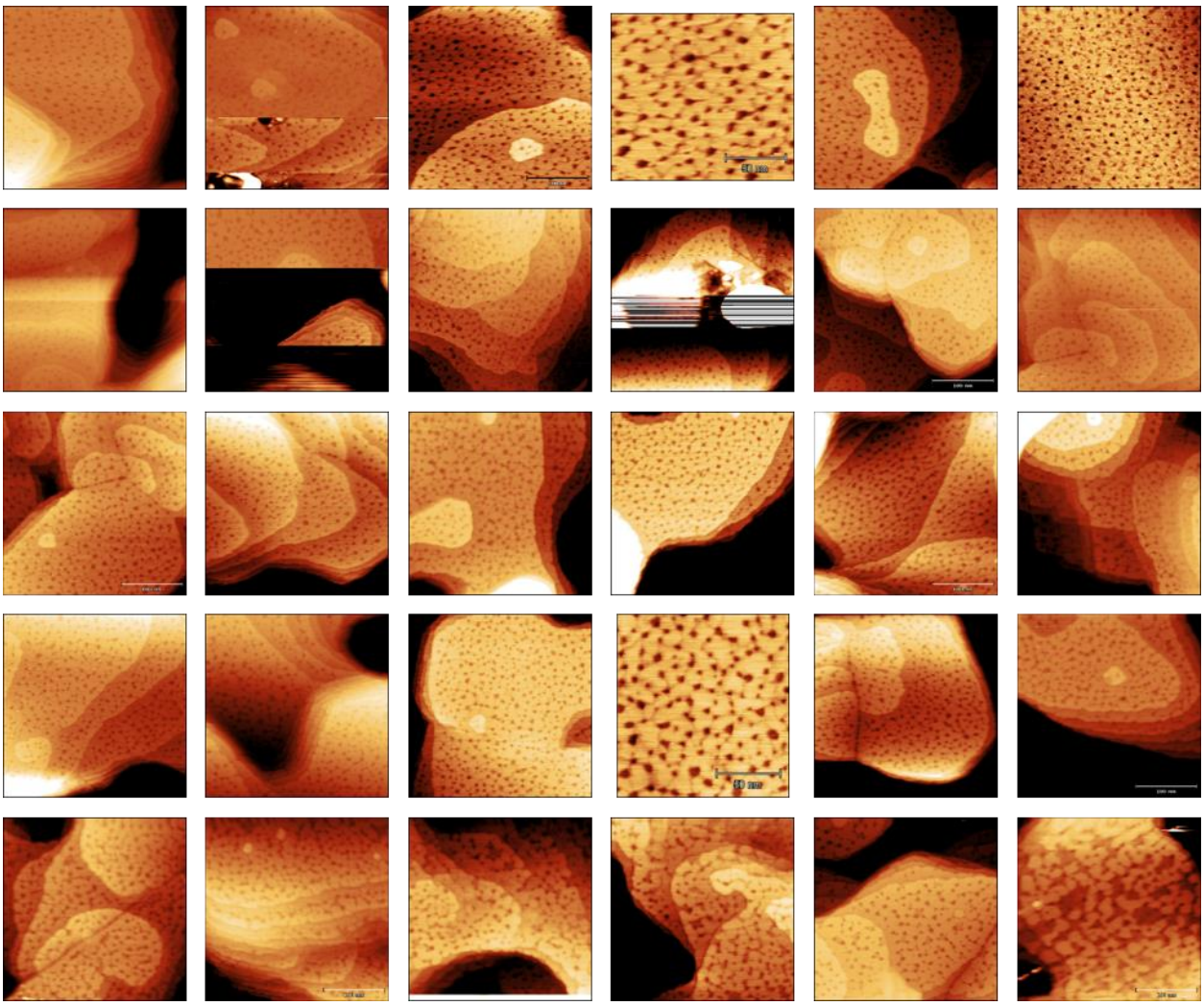

These are the first 30 images used in constructing the 10 carbon plot in **Figure 3.6** that was acquired at the same time as the 9C reaction

Figure A2.5 (con)

Directory: Appendix\9_10C Run\10C

Filenames: Starting at top left, going across the rows:
2018_03_28_split_sample2_10C_unreactred0003
2018_03_28_split_sample2_10C_10min0007
2018_03_28_split_sample2_10C_10min0009
2018_03_28_split_sample2_10C_10min0012
2018_03_28_split_sample2_10C_10min0020
2018_03_29_split_sample2_10C_20min0009
2018_03_29_split_sample2_10C_20min0014
2018_03_29_split_sample2_10C_20min0017
2018_03_29_split_sample2_10C_20min0022
2018_03_29_split_sample2_10C_20min0027
2018_03_30_split_sample2_10C_25min0011
2018_03_30_split_sample2_10C_25min0012
2018_04_01_split_sample2_10C_25min0001
2018_04_01_split_sample2_10C_30min0010
2018_04_01_split_sample2_10C_30min0013
2018_04_01_split_sample2_10C_30min0014
2018_04_01_split_sample2_10C_30min0017
2018_04_02_split_sample2_10C_35min0009
2018_04_03_split_sample2_10C_35min0002
2018_04_03_split_sample2_10C_35min0005
2018_04_03_split_sample2_10C_40min0009
2018_04_03_split_sample2_10C_40min0018
2018_04_03_split_sample2_10C_45min0041
2018_04_03_split_sample2_10C_45min0043
2018_04_04_split_sample2_10C_50min0020
2018_04_04_split_sample2_10C_50min0021
2018_04_05_split_sample2_10C_50min0009
2018_04_05_split_sample2_10C_55min0012

Figure A2.6

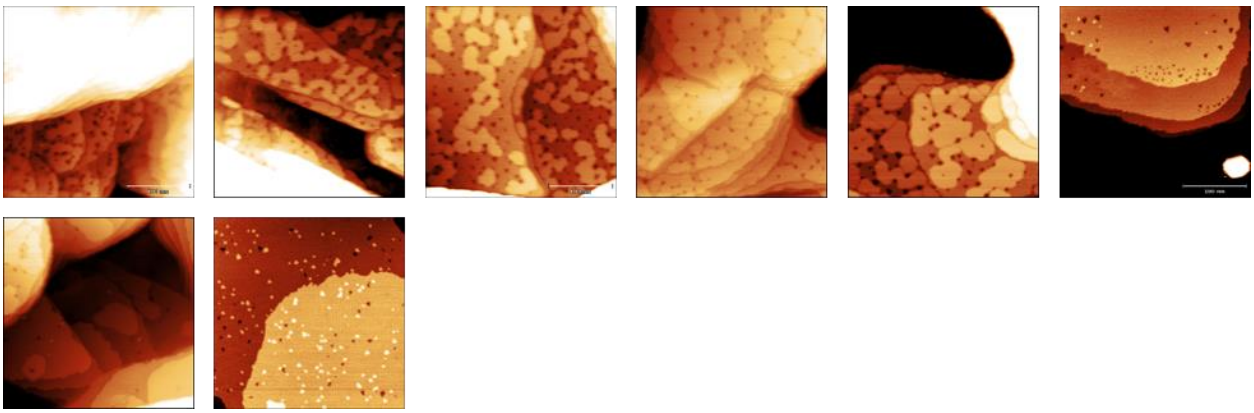

These are the final 8 images used in constructing the 10 carbon plot in **Figure 3.6** that was acquired at the same time as the 9C reaction

Directory: Appendix\9_10C Run\10C

Filenames: Starting at top left, going across the rows:
2018_04_05_split_sample2_10C_55min0018
2018_04_05_split_sample2_10C_60min0032
2018_04_05_split_sample2_10C_60min0038
2018_04_09_split_sample2_10C_60min0003
2018_04_09_split_sample2_10C_60min0007
2018_04_09_split_sample2_10C_65min0023
2018_04_10_split_sample2_10C_65min0002
2018_04_11_split_sample2_10C_70min0001

Figure A2.7

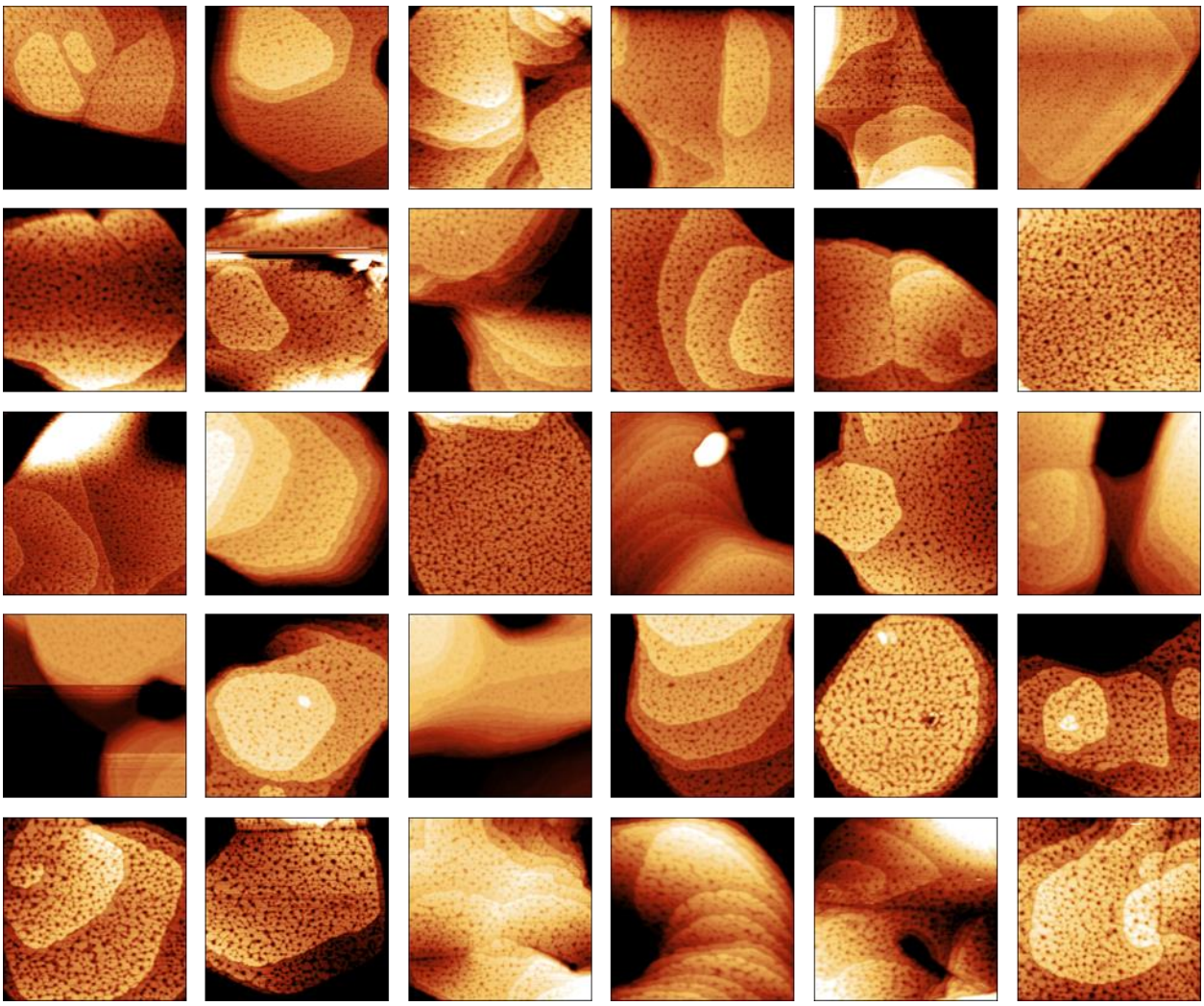

These are the first 30 images used in constructing the 11 carbon plot in **Figure 3.6**

Figure A2.7 (con)

Directory: Appendix\11_10C Run\11C

Filenames: Starting at top left, going across the rows:
2018_05_11_5SplitCrystal_11C_0min0004
2018_05_14_5SplitCrystal_11C_0min0008
2018_05_14_5SplitCrystal_11C_0min0013
2018_05_15_5SplitCrystal_11C_15min0020
2018_05_15_5SplitCrystal_11C_15min0022
2018_05_15_5SplitCrystal_11C_15min0027
2018_05_15_5SplitCrystal_11C_15min0036
2018_05_15_5SplitCrystal_11C_15min0040
2018_05_15_5SplitCrystal_11C_15min0045
2018_05_15_5SplitCrystal_11C_15min0047
2018_05_16_5SplitCrystal_11C_15min0002
2018_05_16_5SplitCrystal_11C_20min0038
2018_05_16_5SplitCrystal_11C_20min0042
2018_05_17_5SplitCrystal_11C_20min0001
2018_05_17_5SplitCrystal_11C_20min0007
2018_05_17_5SplitCrystal_11C_25min0036
2018_05_17_5SplitCrystal_11C_25min0040
2018_05_17_5SplitCrystal_11C_25min0042
2018_05_17_5SplitCrystal_11C_25min0043
2018_05_18_5SplitCrystal_11C_25min0002
2018_05_18_5SplitCrystal_11C_25min0003
2018_05_18_5SplitCrystal_11C_25min0005
2018_05_18_5SplitCrystal_11C_30min0022
2018_05_18_5SplitCrystal_11C_30min0025
2018_05_18_5SplitCrystal_11C_30min0027
2018_05_18_5SplitCrystal_11C_30min0029
2018_05_18_5SplitCrystal_11C_30min0032
2018_05_21_5SplitCrystal_11C_35min0016
2018_05_21_5SplitCrystal_11C_35min0021
2018_05_21_5SplitCrystal_11C_35min0023

Figure A2.8

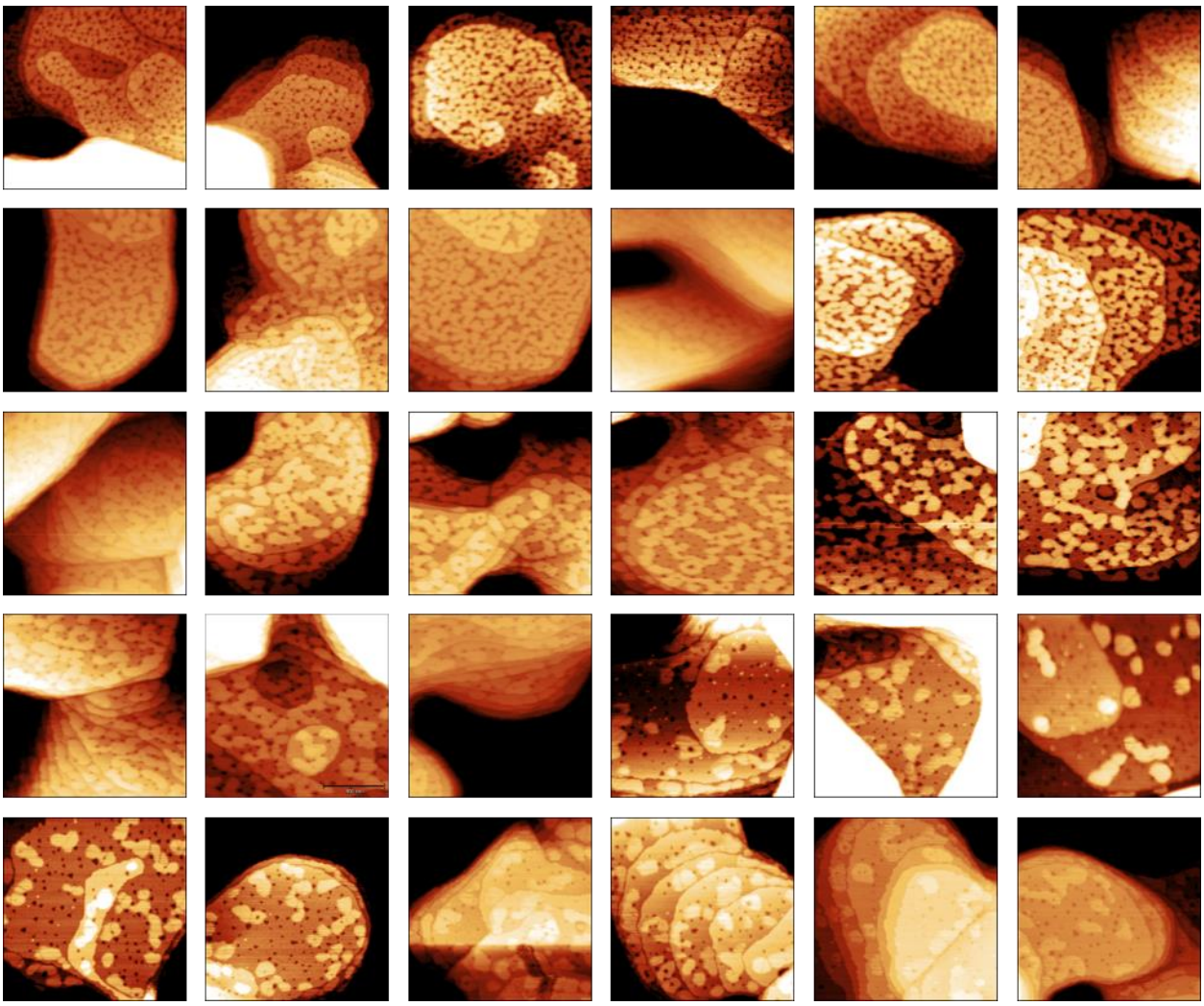

These are the final 30 images used in constructing the 11 carbon plot in **Figure 3.6**

Figure A2.8 (con)

Directory: Appendix\11_10C Run\11C

Filenames: Starting at top left, going across the rows:
2018_05_21_5SplitCrystal_11C_35min0024
2018_05_22_5SplitCrystal_11C_35min0002
2018_05_22_5SplitCrystal_11C_35min0004
2018_05_23_5SplitCrystal_11C_40min0002
2018_05_23_5SplitCrystal_11C_40min0004
2018_05_23_5SplitCrystal_11C_40min0005
2018_05_24_5SplitCrystal_11C_45min0008
2018_05_24_5SplitCrystal_11C_45min0011
2018_05_24_5SplitCrystal_11C_45min0014
2018_05_24_5SplitCrystal_11C_45min0015
2018_05_24_5SplitCrystal_11C_45min0016
2018_05_24_5SplitCrystal_11C_45min0018
2018_05_24_5SplitCrystal_11C_45min0019
2018_05_25_5SplitCrystal_11C_50min0003
2018_05_25_5SplitCrystal_11C_50min0005
2018_05_25_5SplitCrystal_11C_50min0006
2018_05_25_5SplitCrystal_11C_50min0008
2018_05_25_5SplitCrystal_11C_50min0011
2018_05_25_5SplitCrystal_11C_50min0012
2018_05_25_5SplitCrystal_11C_50min0013
2018_05_25_5SplitCrystal_11C_50min0014
2018_05_28_5SplitCrystal_11C_55min0003
2018_05_28_5SplitCrystal_11C_55min0004
2018_05_28_5SplitCrystal_11C_55min0008
2018_05_28_5SplitCrystal_11C_55min0010
2018_05_28_5SplitCrystal_11C_55min0011
2018_05_28_5SplitCrystal_11C_55min0012
2018_05_28_5SplitCrystal_11C_55min0014
2018_05_28_5SplitCrystal_11C_55min0015
2018_05_28_5SplitCrystal_11C_55min0016

Figure A2.9

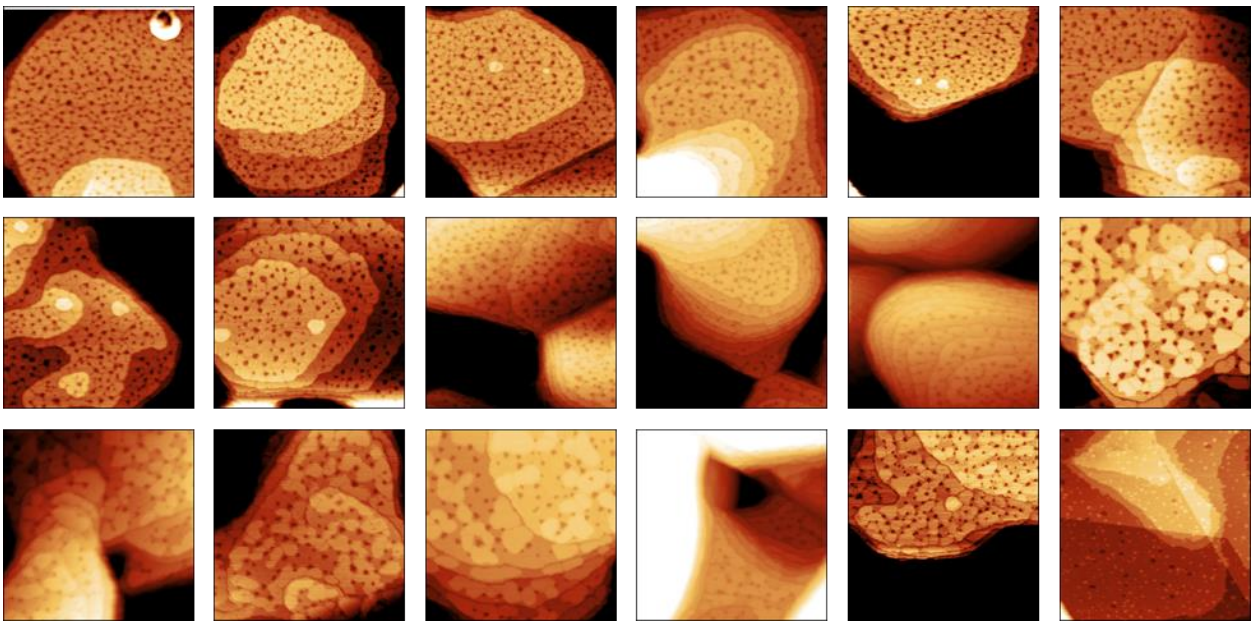

These are the images used in constructing the 10 carbon plot in **Figure 3.6** that was acquired at the same time as the 8C reaction

Figure A2.9 (con)

Directory: Appendix\11_10C Run\10C

Filenames: Starting at top left, going across the rows:
2018_05_24_5SplitCrystal_10C_45min0006
2018_05_10_5SplitCrystal_10C_0min0001
2018_05_11_5SplitCrystal_10C_0min0014
2018_05_14_5SplitCrystal_10C_0min0004
2018_05_15_5SplitCrystal_10C_15min0002
2018_05_15_5SplitCrystal_10C_15min0003
2018_05_16_5SplitCrystal_10C_20min0012
2018_05_16_5SplitCrystal_10C_20min0018
2018_05_16_5SplitCrystal_10C_20min0023
2018_05_17_5SplitCrystal_10C_25min0010
2018_05_17_5SplitCrystal_10C_25min0015
2018_05_18_5SplitCrystal_10C_30min0010
2018_05_21_5SplitCrystal_10C_30min0002
2018_05_21_5SplitCrystal_10C_35min0005
2018_05_21_5SplitCrystal_10C_35min0007
2018_05_21_5SplitCrystal_10C_35min0012
2018_05_21_5SplitCrystal_10C_35min0014
2018_05_22_5SplitCrystal_10C_40min0006

Figure A2.10

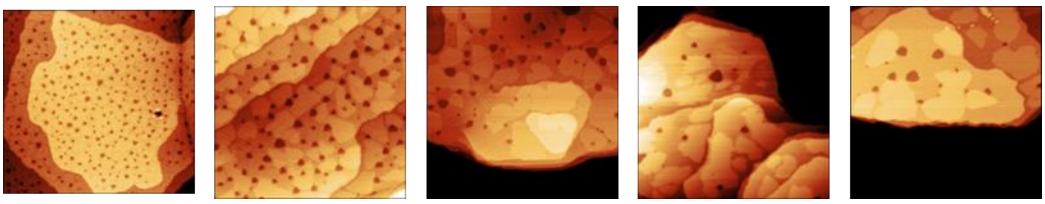

These are the images where the etch pits were measured and used to create the histograms in **Figure 3.9** from the 8-carbon SAM

Directory: Appendix\EtchPits\8C

Filenames: Starting at top left, going across the rows:
2018_04_17_SplitCrystal_8C_0min0010
2018_04_20_SplitCrystal_8C_10min0026
2018_04_18_SplitCrystal_8C_8min0038
2018_04_19_SplitCrystal_8C_10min0018
2018_04_20_SplitCrystal_8C_10min0025

Figure A2.11

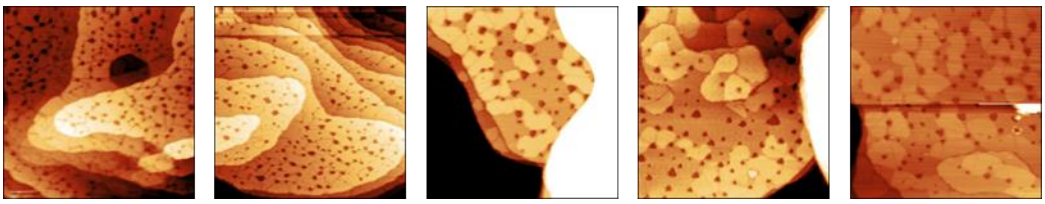

These are the images where the etch pits were measured and used to create the histograms in **Figure 3.9** from the 9-carbon SAM

Directory: Appendix\EtchPits\9C

Filenames: Starting at top left, going across the rows:
2018_03_28_split_sample2_9C_unreactred0005
2018_03_29_split_sample2_9C_10min0001
2018_04_04_split_sample2_9C_45min0007
2018_04_03_split_sample2_9C_45min0048
2018_04_03_split_sample2_9C_45min0050

Figure A2.12

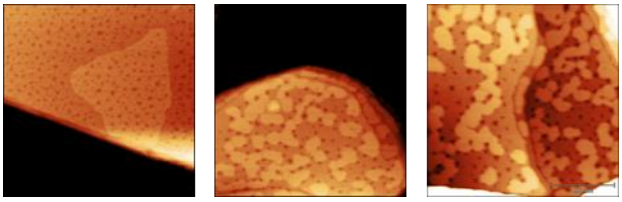

These are the images where the etch pits were measured and used to create the histograms in **Figure 3.9** from the 10-carbon SAM

Directory: Appendix\EtchPits\10C

Filenames: Starting at top left, going across the rows:
2018_04_17_SplitCrystal_10C_0min0022
2018_04_05_split_sample2_10C_60min0036
2018_04_05_split_sample2_10C_60min0038

Figure A2.13

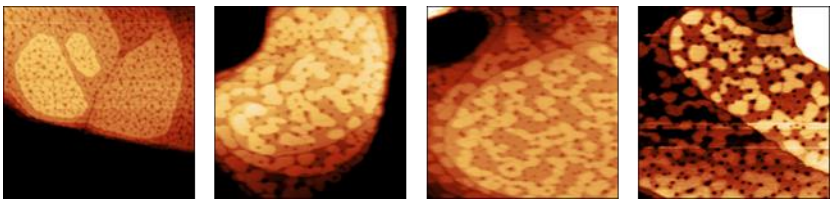

These are the images where the etch pits were measured and used to create the histograms in **Figure 3.9** from the 11-carbon SAM

Directory: Appendix\EtchPits\11C

Filenames: Starting at top left, going across the rows:
2018_05_11_5SplitCrystal_11C_0min0004
2018_05_25_5SplitCrystal_11C_50min0006
2018_05_25_5SplitCrystal_11C_50min0008
2018_05_25_5SplitCrystal_11C_50min0003

Figure A2.14

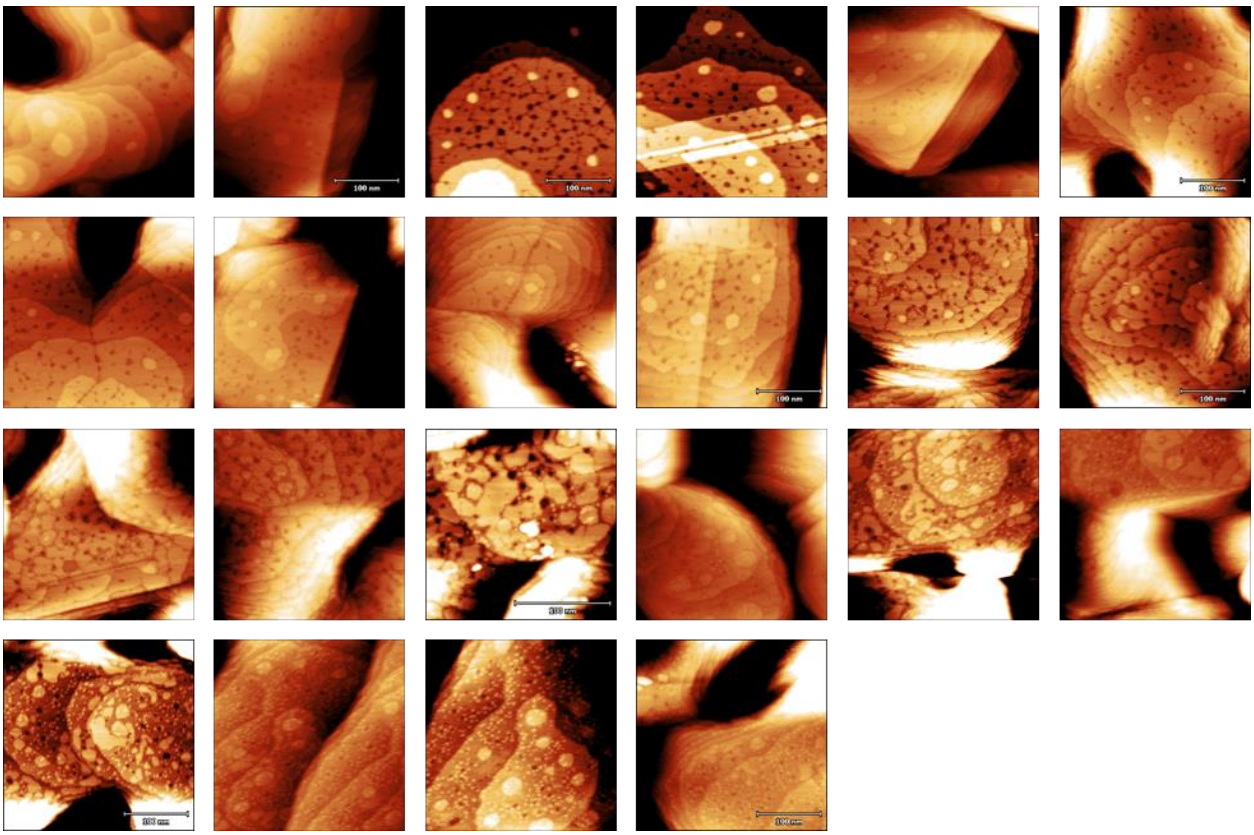

These are the images used in constructing the 250 K plot in **Figure 4.4**

Figure A2.14 (con)

Directory: Appendix\250K

Filenames: Starting at top left, going across the rows:
2018_12_10_SAM_60min_250K_ImagedRT0001
2018_12_10_SAM_60min_250K_ImagedRT0004
2018_12_10_SAM_90min_250K_Imaged250K0015
2018_12_10_SAM_90min_250K_Imaged250K0025
2018_12_10_SAM_90min_250K_Imaged250K0028
2018_12_10_SAM_105min_250K_Imaged250K0034
2018_12_10_SAM_105min_250K_Imaged250K0040
2018_12_11_SAM_105min_250K_Imaged250K0001
2018_12_11_SAM_120min_250K_Imaged250K0009
2018_12_11_SAM_120min_250K_Imaged250K0018
2018_12_11_SAM_135min_250K_Imaged250K0024
2018_12_11_SAM_135min_250K_Imaged250K0028
2018_12_11_SAM_135min_250K_Imaged250K0032
2018_12_11_SAM_150min_250K_Imaged250K0043
2018_12_12_SAM_165min_250K_Imaged250K0001
2018_12_12_SAM_165min_250K_Imaged250K0005
2018_12_12_SAM_165min_250K_Imaged250K0011
2018_12_12_SAM_180min_250K_Imaged250K0013
2018_12_12_SAM_180min_250K_Imaged250K0015
2018_12_12_SAM_195min_250K_Imaged250K0031

Figure A2.15

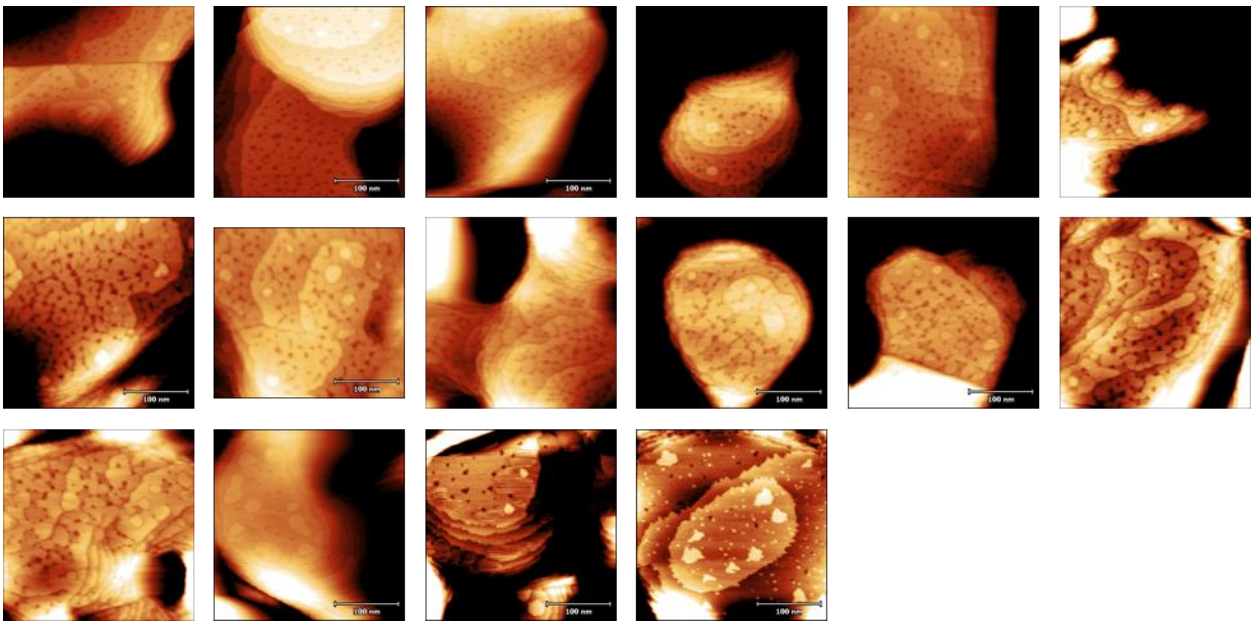

These are the images used in constructing the 270 K plot in **Figure 4.4**

Directory: Appendix\270K

Filenames: Starting at top left, going across the rows:
2018_12_20_SAM_0min_RT0006
2018_12_20_SAM_0min_RT0017
2018_12_20_SAM_60min_270k0028
2018_12_20_SAM_60min_270k0029
2018_12_20_SAM_60min_270k0035
2018_12_20_SAM_75min_270k0040
2018_12_20_SAM_75min_270k0043
2018_12_20_SAM_75min_270k0045
2018_12_20_SAM_75min_270k0049
2018_12_20_SAM_90min_270k0051
2018_12_20_SAM_90min_270k0052
2018_12_20_SAM_90min_270k0054
2018_12_20_SAM_90min_270k0056
2018_12_21_SAM_105min_270k0004
2018_12_21_SAM_105min_270k0008
2018_12_21_SAM_120min_270k0014

Figure A2.16

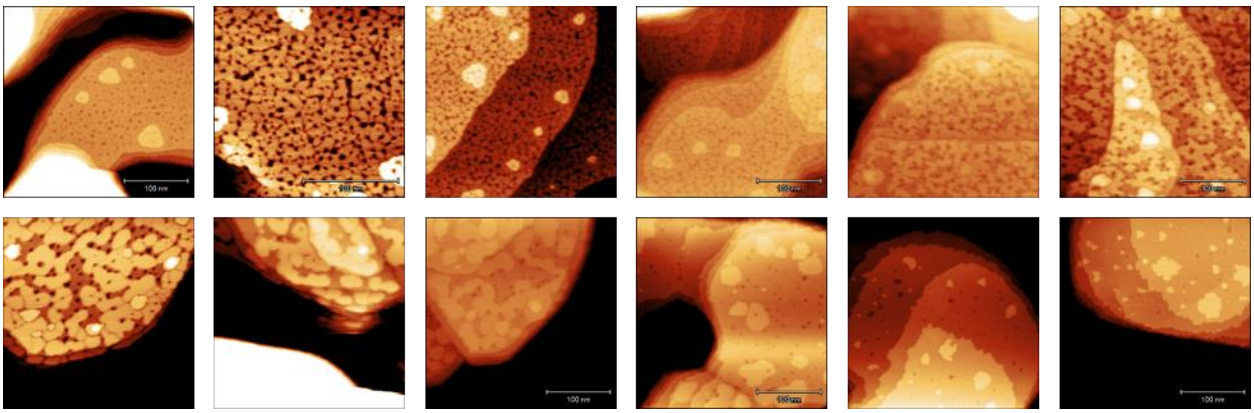

These are the images used in constructing the room temperature plot in **Figure 4.4**

Directory: Appendix\Room_Temp

Filenames: Starting at top left, going across the rows:
2018_11_20_10CSAM0016
2018_11_21_10CSAM_20min_reaction0005
2018_11_21_10CSAM_20min_reaction0011
2018_11_21_10CSAM_30min_reaction0023
2018_11_21_10CSAM_40min_reaction0032
2018_11_21_10CSAM_40min_reaction0038
2018_11_25_10CSAM_40min_reaction0000
2018_11_25_10CSAM_45min_reaction0002
2018_11_25_10CSAM_45min_reaction0004
2018_11_25_10CSAM_50min_reaction0006
2018_11_25_10CSAM_50min_reaction0008
2018_11_25_10CSAM_55min_reaction0015

Reference List

(1) Thompson, R. S.; Langlois, G. G.; Sibener, S. J. Oxidative Destruction of Multilayer Diisopropyl Methylphosphonate Films by O(3P) Atomic Oxygen. *J. Phys. Chem. B* **2018**, *122* (2), 455–463. https://doi.org/10.1021/acs.jpcb.7b02589.

(2) Langlois, G. G.; Thompson, R. S.; Li, W.; Sibener, S. J. Oxidation, Destruction, and Persistence of Multilayer Dimethyl Methylphosphonate Films during Exposure to O(3P) Atomic Oxygen. *J. Phys. Chem. C* **2016**, *120* (30), 16863–16870. https://doi.org/10.1021/acs.jpcc.6b05880.

(3) Kluth, G. J.; Sung, M. M.; Maboudian, R. Interaction of H(D) Atoms with Octadecylsiloxane Self-Assembled Monolayers on the Si(100) Surface. *Langmuir* **1997**, *13* (24), 6491–6496. https://doi.org/10.1021/la970641g.

(4) Paz, Y.; Trakhtenberg, S.; Naaman, R. Destruction of Organized Organic Monolayers by Oxygen Atoms. *J. Phys. Chem.* **1992**, *96* (26), 10964–10967. https://doi.org/10.1021/j100205a066.

(5) Torres, J.; Perry, C. C.; Wagner, A. J.; Fairbrother, D. H. Interaction of Chlorine Radicals with Polyethylene and Hydrocarbon Thin Films under Vacuum Conditions—a Comparison with Atomic Oxygen Reactivity. *Surface Science* **2003**, *543* (1), 75–86. https://doi.org/10.1016/S0039-6028(03)00992-0.

(6) Hopf, C.; von Keudell, A.; Jacob, W. Chemical Sputtering of Hydrocarbon Films. *Journal of Applied Physics* **2003**, *94* (4), 2373–2380. https://doi.org/10.1063/1.1594273.

(7) Bürgi, T.; Trautman, T. R.; Gostein, M.; Lahr, D. L.; Haug, K. L.; Ceyer, S. T. Reactions of Gas Phase H Atoms with Ethylene, Acetylene and Ethane Adsorbed on Ni(111). *Surface Science* **2002**, *501* (1), 49–73. https://doi.org/10.1016/S0039-6028(01)01755-1.

(8) Zhang, J.; Upadhyaya, H. P.; Brunsvold, A. L.; Minton, T. K. Hyperthermal Reactions of O and O_2 with a Hydrocarbon Surface: Direct C−C Bond Breakage by O and H-Atom Abstraction by O_2. *The Journal of Physical Chemistry B* **2006**, *110* (25), 12500–12511. https://doi.org/10.1021/jp061521x.

(9) Zhang, J.; Garton, D. J.; Minton, T. K. Reactive and Inelastic Scattering Dynamics of Hyperthermal Oxygen Atoms on a Saturated Hydrocarbon Surface. *J. Chem. Phys.* **2002**, *117* (13), 6239–6251. https://doi.org/10.1063/1.1460858.

(10) Gologan, B.; Green, J. R.; Alvarez, J.; Laskin, J.; Cooks, R. G. Ion/Surface Reactions and Ion Soft-Landing. *Phys. Chem. Chem. Phys.* **2005**, *7* (7), 1490–1500. https://doi.org/10.1039/B418056A.

(11) Sieval, A. B.; Huisman, C. L.; Schönecker, A.; Schuurmans, F. M.; van der Heide, A. S. H.; Goossens, A.; Sinke, W. C.; Zuilhof, H.; Sudhölter, E. J. R. Silicon Surface Passivation by Organic Monolayers: Minority Charge Carrier Lifetime Measurements and Kelvin Probe Investigations. *J. Phys. Chem. B* **2003**, *107* (28), 6846–6852. https://doi.org/10.1021/jp034314v.

(12) Gorham, J.; Smith, B.; Fairbrother, D. H. Modification of Alkanethiolate Self-Assembled Monolayers by Atomic Hydrogen: Influence of Alkyl Chain Length. *J. Phys. Chem. C* **2007**, *111* (1), 374–382. https://doi.org/10.1021/jp0646224.

(13) Tasić, U. S.; Yan, T.; Hase, W. L. Dynamics of Energy Transfer in Collisions of O(3P) Atoms with a 1-Decanethiol Self-Assembled Monolayer Surface. *J. Phys. Chem. B* **2006**, *110* (24), 11863–11877. https://doi.org/10.1021/jp0611065.

(14) Troya, D.; Schatz, G. C. Theoretical Studies of Hyperthermal O(3P) Collisions with Hydrocarbon Self-Assembled Monolayers. *J. Chem. Phys.* **2004**, *120* (16), 7696–7707. https://doi.org/10.1063/1.1688312.

(15) Wagner, A. J.; Wolfe, G. M.; Fairbrother, D. H. Atomic Oxygen Reactions with Semifluorinated and N-Alkanethiolate Self-Assembled Monolayers. *J. Chem. Phys.* **2004**, *120* (8), 3799–3810. https://doi.org/10.1063/1.1640336.

(16) Lee, D. Y.; Kautz, N. A.; Kandel, S. A. Reactivity of Gas-Phase Radicals with Organic Surfaces. *J. Phys. Chem. Lett.* **2013**, *4* (23), 4103–4112. https://doi.org/10.1021/jz401691w.

(17) Lee, D. Y.; Jobbins, M. M.; Gans, A. R.; Kandel, S. A. The Role of Defects in the Reaction of Chlorine Atoms with Alkanethiol Self-Assembled Monolayers. *Phys. Chem. Chem. Phys.* **2013**, *15* (43), 18844–18854. https://doi.org/10.1039/C3CP52023D.

(18) Kautz, N. A.; Kandel, S. A. Alkanethiol/Au(111) Self-Assembled Monolayers Contain Gold Adatoms: Scanning Tunneling Microscopy before and after Reaction with Atomic Hydrogen. *J. Am. Chem. Soc.* **2008**, *130* (22), 6908–6909. https://doi.org/10.1021/ja8011325.

(19) Kautz, N. A.; Kandel, S. A. Alkanethiol Monolayers Contain Gold Adatoms, and Adatom Coverage Is Independent of Chain Length. *J. Phys. Chem. C* **2009**, *113* (44), 19286–19291. https://doi.org/10.1021/jp907846u.

(20) Kautz, N. A.; Fogarty, D. P.; Kandel, S. A. Degradation of Octanethiol Self-Assembled Monolayers from Hydrogen-Atom Exposure: A Molecular-Scale Study Using Scanning Tunneling Microscopy. *Surface Science* **2007**, *601* (15), L86–L90. https://doi.org/10.1016/j.susc.2007.05.051.

(21) Kautz, N. A.; Kandel, S. A. Reactivity of Self-Assembled Monolayers: Local Surface Environment Determines Monolayer Erosion Rates. *J. Phys. Chem. C* **2012**, *116* (7), 4725–4731. https://doi.org/10.1021/jp211209m.

(22) Poirier, G. E.; Tarlov, M. J. Molecular Ordering and Gold Migration Observed in Butanethiol Self-Assembled Monolayers Using Scanning Tunneling Microscopy. *The Journal of Physical Chemistry* **1995**, *99* (27), 10966–10970. https://doi.org/10.1021/j100027a042.

(23) Yuan, H.; Gibson, K. D.; Li, W.; Sibener, S. J. Modification of Alkanethiolate Monolayers by O(3P) Atomic Oxygen: Effect of Chain Length and Surface Temperature. *J. Phys. Chem. B* **2013**, *117* (16), 4381–4389. https://doi.org/10.1021/jp307005x.

(24) Nuzzo, R. G.; Allara, D. L. Adsorption of Bifunctional Organic Disulfides on Gold Surfaces. *J. Am. Chem. Soc.* **1983**, *105* (13), 4481–4483. https://doi.org/10.1021/ja00351a063.

(25) Poirier, G. E.; Pylant, E. D. The Self-Assembly Mechanism of Alkanethiols on Au(111). *Science* **1996**, *272* (5265), 1145–1148. https://doi.org/10.1126/science.272.5265.1145.

(26) Poirier, G. E. Characterization of Organosulfur Molecular Monolayers on Au(111) Using Scanning Tunneling Microscopy. *Chem. Rev.* **1997**, *97* (4), 1117–1128. https://doi.org/10.1021/cr960074m.

(27) Poirier, G. E.; Tarlov, M. J. The c(4X2) Superlattice of n-Alkanethiol Monolayers Self-Assembled on Au(111). *Langmuir* **1994**, *10* (9), 2853–2856. https://doi.org/10.1021/la00021a001.

(28) Poirier, G. E. Coverage-Dependent Phases and Phase Stability of Decanethiol on Au(111). *Langmuir* **1999**, *15* (4), 1167–1175. https://doi.org/10.1021/la981374x.

(29) Fitts, W. P.; White, J. M.; Poirier, G. E. Low-Coverage Decanethiolate Structure on Au(111): Substrate Effects. *Langmuir* **2002**, *18* (5), 1561–1566. https://doi.org/10.1021/la0107650.

(30) Poirier, G. E. Mechanism of Formation of Au Vacancy Islands in Alkanethiol Monolayers on Au(111). *Langmuir* **1997**, *13* (7), 2019–2026. https://doi.org/10.1021/la960777z.

(31) Nakayama, M.; Kautz, N. A.; Wang, T.; Sibener, S. J. Formation of Rectangular Packing and One-Dimensional Lines of C60 on 11-Phenoxyundecanethiol Self-Assembled Monolayers on Au(111). *Langmuir* **2012**, *28* (10), 4694–4701. https://doi.org/10.1021/la204986n.

(32) Nakayama, M.; Kautz, N. A.; Wang, T.; Yuan, H.; Sibener, S. J. Structural Investigations of the (5×√3) Striped Phase of Annealed 11-Phenoxy Undecanethiol Self-Assembled Monolayers on Au(111). *J. Phys. Chem. C* **2012**, *116* (10), 6298–6306. https://doi.org/10.1021/jp212193v.

(33) Chesneau, F.; Schüpbach, B.; Szelągowska-Kunstman, K.; Ballav, N.; Cyganik, P.; Terfort, A.; Zharnikov, M. Self-Assembled Monolayers of Perfluoroterphenyl-Substituted Alkanethiols: Specific Characteristics and Odd–Even Effects. *Phys. Chem. Chem. Phys.* **2010**, *12* (38), 12123–12137. https://doi.org/10.1039/C0CP00317D.

(34) Holmlin, R. E.; Chen, X.; Chapman, R. G.; Takayama, S.; Whitesides, G. M. Zwitterionic SAMs That Resist Nonspecific Adsorption of Protein from Aqueous Buffer. *Langmuir* **2001**, *17* (9), 2841–2850. https://doi.org/10.1021/la0015258.

(35) Ziemba, C.; Khavkin, M.; Priftis, D.; Acar, H.; Mao, J.; Benami, M.; Gottlieb, M.; Tirrell, M.; Kaufman, Y.; Herzberg, M. Antifouling Properties of a Self-Assembling Glutamic Acid-Lysine Zwitterionic Polymer Surface Coating. *Langmuir* **2019**, *35* (5), 1699–1713. https://doi.org/10.1021/acs.langmuir.8b00181.

(36) Woodruff, D. P. The Role of Reconstruction in Self-Assembly of Alkylthiolate Monolayers on Coinage Metal Surfaces. *Applied Surface Science* **2007**, *254* (1), 76–81. https://doi.org/10.1016/j.apsusc.2007.07.081.

(37) Yu, M.; Bovet, N.; Satterley, C. J.; Bengió, S.; Lovelock, K. R. J.; Milligan, P. K.; Jones, R. G.; Woodruff, D. P.; Dhanak, V. True Nature of an Archetypal Self-Assembly System: Mobile Au-Thiolate Species on Au(111). *Phys. Rev. Lett.* **2006**, *97* (16), 166102. https://doi.org/10.1103/PhysRevLett.97.166102.

(38) Maksymovych, P.; Sorescu, D. C.; Yates, J. T. Gold-Adatom-Mediated Bonding in Self-Assembled Short-Chain Alkanethiolate Species on the Au(111) Surface. *Phys. Rev. Lett.* **2006**, *97* (14), 146103. https://doi.org/10.1103/PhysRevLett.97.146103.

(39) Mazzarello, R.; Cossaro, A.; Verdini, A.; Rousseau, R.; Casalis, L.; Danisman, M. F.; Floreano, L.; Scandolo, S.; Morgante, A.; Scoles, G. Structure of a CH_3S Monolayer on Au(111) Solved by the Interplay between Molecular Dynamics Calculations and Diffraction Measurements. *Phys. Rev. Lett.* **2007**, *98* (1), 016102. https://doi.org/10.1103/PhysRevLett.98.016102.

(40) Cossaro, A.; Mazzarello, R.; Rousseau, R.; Casalis, L.; Verdini, A.; Kohlmeyer, A.; Floreano, L.; Scandolo, S.; Morgante, A.; Klein, M. L.; et al. X-Ray Diffraction and Computation Yield the Structure of Alkanethiols on Gold(111). *Science* **2008**, *321* (5891), 943–946. https://doi.org/10.1126/science.1158532.

(41) Chaudhuri, A.; Lerotholi, T. J.; Jackson, D. C.; Woodruff, D. P.; Dhanak, V. Local Methylthiolate Adsorption Geometry on Au(111) from Photoemission Core-Level Shifts. *Phys. Rev. Lett.* **2009**, *102* (12), 126101. https://doi.org/10.1103/PhysRevLett.102.126101.

(42) Chaudhuri, A.; Lerotholi, T. J.; Jackson, D. C.; Woodruff, D. P.; Jones, R. G. ($2\sqrt{3} \times 3$)rect. Phase of Alkylthiolate Self-Assembled Monolayers on Au(111): A Symmetry-Constrained Structural Solution. *Phys. Rev. B* **2009**, *79* (19), 195439. https://doi.org/10.1103/PhysRevB.79.195439.

(43) Jackson, D. C.; Chaudhuri, A.; Lerotholi, T. J.; Woodruff, D. P.; Jones, R. G.; Dhanak, V. R. The Local Adsorption Site of Methylthiolate on Au(111): Bridge or Atop? *Surface Science* **2009**, *603* (5), 807–813. https://doi.org/10.1016/j.susc.2009.01.022.

(44) Chaudhuri, A.; Odelius, M.; Jones, R. G.; Lee, T.-L.; Detlefs, B.; Woodruff, D. P. The Structure of the Au(111)/Methylthiolate Interface: New Insights from near-Edge x-Ray Absorption Spectroscopy and x-Ray Standing Waves. *J. Chem. Phys.* **2009**, *130* (12), 124708. https://doi.org/10.1063/1.3102095.

(45) Woodruff, D. P. The Interface Structure of N-Alkylthiolate Self-Assembled Monolayers on Coinage Metal Surfaces. *Phys. Chem. Chem. Phys.* **2008**, *10* (48), 7211–7221. https://doi.org/10.1039/B813948B.

(46) Camillone, N.; Eisenberger, P.; Leung, T. Y. B.; Schwartz, P.; Scoles, G.; Poirier, G. E.; Tarlov, M. J. New Monolayer Phases of N-alkane Thiols Self-assembled on Au(111): Preparation, Surface Characterization, and Imaging. *The Journal of Chemical Physics* **1994**, *101* (12), 11031–11036. https://doi.org/10.1063/1.467854.

(47) Binnig, G.; Rohrer, H.; Gerber, Ch.; Weibel, E. Surface Studies by Scanning Tunneling Microscopy. *Phys. Rev. Lett.* **1982**, *49* (1), 57–61. https://doi.org/10.1103/PhysRevLett.49.57.

(48) Hamers, R. J. Scanned Probe Microscopies in Chemistry. *J. Phys. Chem.* **1996**, *100* (31), 13103–13120. https://doi.org/10.1021/jp960054o.

(49) Binnig, G.; Rohrer, H. Scanning Tunneling Microscopy—from Birth to Adolescence. *Reviews of Modern Physics* **1987**, *59* (3), 615–625. https://doi.org/10.1103/RevModPhys.59.615.

(50) Binnig, G.; Rohrer, H.; Gerber, Ch.; Weibel, E. 7 by 7 Reconstruction on Si(111) Resolved in Real Space. *Phys. Rev. Lett.* **1983**, *50* (2), 120–123. https://doi.org/10.1103/PhysRevLett.50.120.

(51) Hipps, K. W. SCANNING TUNNELING SPECTROSCOPY (STS). In *Handbook of Applied Solid State Spectroscopy*; Vij, D. R., Ed.; Springer US: Boston, MA, 2006; pp 305–350. https://doi.org/10.1007/0-387-37590-2_7.

(52) Wang, T.; Vaxenburg, R.; Liu, W.; Rupich, S. M.; Lifshitz, E.; Efros, A. L.; Talapin, D. V.; Sibener, S. J. Size-Dependent Energy Levels of InSb Quantum Dots Measured by Scanning Tunneling Spectroscopy. *ACS Nano* **2015**, *9* (1), 725–732. https://doi.org/10.1021/nn5061805.

(53) Wang, T. CONDUCTIVE ATOMIC FORCE MICROSCOPY STUDY OF SINGLE SEMICONDUCTOR QUANTUM DOTS AND QUANTUM DOT AGGREGATES, University of Chicago: Chicago, IL, 2014.

(54) Zharnikov, M.; Geyer, W.; Gölzhäuser, A.; Frey, S.; Grunze, M. Modification of Alkanethiolate Monolayers on Au-Substrate by Low Energy Electron Irradiation: Alkyl Chains and the S/Au Interface. *Phys. Chem. Chem. Phys.* **1999**, *1* (13), 3163–3171. https://doi.org/10.1039/A902013F.

(55) Willey, T. M.; Vance, A. L.; van Buuren, T.; Bostedt, C.; Terminello, L. J.; Fadley, C. S. Rapid Degradation of Alkanethiol-Based Self-Assembled Monolayers on Gold in Ambient Laboratory Conditions. *Surface Science* **2005**, *576* (1), 188–196. https://doi.org/10.1016/j.susc.2004.12.022.

(56) Nečas, D.; Klapetek, P. Gwyddion: An Open-Source Software for SPM Data Analysis. *Central European Journal of Physics* **2012**, *10* (1), 181–188. https://doi.org/10.2478/s11534-011-0096-2.

(57) Ulman, A. Formation and Structure of Self-Assembled Monolayers. *Chem. Rev.* **1996**, *96* (4), 1533–1554. https://doi.org/10.1021/cr9502357.

(58) Häkkinen, H. The Gold–Sulfur Interface at the Nanoscale. *Nature Chemistry* **2012**, *4* (6), 443–455. https://doi.org/10.1038/nchem.1352.

(59) DiMilla, P. A.; Folkers, J. P.; Biebuyck, H. A.; Haerter, R.; Lopez, G. P.; Whitesides, G. M. Wetting and Protein Adsorption on Self-Assembled Monolayers of Alkanethiolates Supported on Transparent Films of Gold. *Journal of the American Chemical Society* **1994**, *116* (5), 2225–2226. https://doi.org/10.1021/ja00084a105.

(60) Meena Devi, J. A Simulation Study on the Thermal and Wetting Behavior of Alkane Thiol SAM on Gold (111) Surface. *Progress in Natural Science: Materials International* **2014**, *24* (4), 405–411. https://doi.org/10.1016/j.pnsc.2014.06.009.

(61) Gleiche, M.; Chi, L. F.; Fuchs, H. Nanoscopic Channel Lattices with Controlled Anisotropic Wetting. *Nature* **2000**, *403* (6766), 173–175. https://doi.org/10.1038/35003149.

(62) Laibinis, P. E.; Whitesides, G. M.; Allara, D. L.; Tao, Y. T.; Parikh, A. N.; Nuzzo, R. G. Comparison of the Structures and Wetting Properties of Self-Assembled Monolayers of n-Alkanethiols on the Coinage Metal Surfaces, Copper, Silver, and Gold. *J. Am. Chem. Soc.* **1991**, *113* (19), 7152–7167. https://doi.org/10.1021/ja00019a011.

(63) Raynor, J. E.; Capadona, J. R.; Collard, D. M.; Petrie, T. A.; García, A. J. Polymer Brushes and Self-Assembled Monolayers: Versatile Platforms to Control Cell Adhesion to Biomaterials (Review). *Biointerphases* **2009**, *4* (2), FA3–FA16. https://doi.org/10.1116/1.3089252.

(64) Kondo, T.; Uosaki, K. Self-Assembled Monolayers (SAMs) with Photo-Functionalities. *Journal of Photochemistry and Photobiology C: Photochemistry Reviews* **2007**, *8* (1), 1–17. https://doi.org/10.1016/j.jphotochemrev.2007.02.001.

(65) Plant, A. L. Self-Assembled Phospholipid/Alkanethiol Biomimetic Bilayers on Gold. *Langmuir* **1993**, *9* (11), 2764–2767. https://doi.org/10.1021/la00035a004.

(66) Prime, K. L.; Whitesides, G. M. Adsorption of Proteins onto Surfaces Containing End-Attached Oligo(Ethylene Oxide): A Model System Using Self-Assembled Monolayers. *J. Am. Chem. Soc.* **1993**, *115* (23), 10714–10721. https://doi.org/10.1021/ja00076a032.

(67) Zamborini, F. P.; Crooks, R. M. Corrosion Passivation of Gold by N-Alkanethiol Self-Assembled Monolayers: Effect of Chain Length and End Group. *Langmuir* **1998**, *14* (12), 3279–3286. https://doi.org/10.1021/la971121o.

(68) Yourdshahyan, Y.; Zhang, H. K.; Rappe, A. M. N-Alkyl Thiol Head-Group Interactions with the Au(111) Surface. *Phys. Rev. B* **2001**, *63* (8), 081405. https://doi.org/10.1103/PhysRevB.63.081405.

(69) Love, J. C.; Estroff, L. A.; Kriebel, J. K.; Nuzzo, R. G.; Whitesides, G. M. Self-Assembled Monolayers of Thiolates on Metals as a Form of Nanotechnology. *Chem. Rev.* **2005**, *105* (4), 1103–1170. https://doi.org/10.1021/cr0300789.

(70) Jobbins, M. M.; Raigoza, A. F.; Kandel, S. A. Adatoms at the Sulfur–Gold Interface in 1-Adamantanethiolate Monolayers, Studied Using Reaction with Hydrogen Atoms and Scanning Tunneling Microscopy. *J. Phys. Chem. C* **2011**, *115* (51), 25437–25441. https://doi.org/10.1021/jp209866c.

(71) Lee, D. Y.; Kautz, N. A.; Kandel, S. A. Reactivity of Gas-Phase Radicals with Organic Surfaces. *J. Phys. Chem. Lett.* **2013**, *4* (23), 4103–4112. https://doi.org/10.1021/jz401691w.

(72) Mantis Deposition LTD. *MGC75 Thermal Gas Cracker Operations Manual*; 2017.

(73) Tao, F.; Bernasek, S. L. Understanding Odd−Even Effects in Organic Self-Assembled Monolayers. *Chem. Rev.* **2007**, *107* (5), 1408–1453. https://doi.org/10.1021/cr050258d.

(74) Wong, S.-S.; Takano, H.; Porter, M. D. Mapping Orientation Differences of Terminal Functional Groups by Friction Force Microscopy. *Anal. Chem.* **1998**, *70* (24), 5209–5212. https://doi.org/10.1021/ac9807870.

(75) Wang, Z.; Chen, J.; Gathiaka, S. M.; Oyola-Reynoso, S.; Thuo, M. Effect of Substrate Morphology on the Odd–Even Effect in Hydrophobicity of Self-Assembled Monolayers. *Langmuir* **2016**, *32* (40), 10358–10367. https://doi.org/10.1021/acs.langmuir.6b01681.

(76) Srivastava, P.; Chapman, W. G.; Laibinis, P. E. Odd−Even Variations in the Wettability of N-Alkanethiolate Monolayers on Gold by Water and Hexadecane: A Molecular Dynamics Simulation Study. *Langmuir* **2005**, *21* (26), 12171–12178. https://doi.org/10.1021/la051535e.

(77) Ramin, L.; Jabbarzadeh, A. Odd–Even Effects on the Structure, Stability, and Phase Transition of Alkanethiol Self-Assembled Monolayers. *Langmuir* **2011**, *27* (16), 9748–9759. https://doi.org/10.1021/la201467b.

(78) Ramin, L.; Jabbarzadeh, A. Effect of Load on Structural and Frictional Properties of Alkanethiol Self-Assembled Monolayers on Gold: Some Odd–Even Effects. *Langmuir* **2012**, *28* (9), 4102–4112. https://doi.org/10.1021/la204701z.

(79) Bumm, L. A.; Arnold, J. J.; Charles, L. F.; Dunbar, T. D.; Allara, D. L.; Weiss, P. S. Directed Self-Assembly to Create Molecular Terraces with Molecularly Sharp Boundaries in Organic Monolayers. *J. Am. Chem. Soc.* **1999**, *121* (35), 8017–8021. https://doi.org/10.1021/ja982157l.